Contrib Mineral Petrol (2013) 165:437–455
DOI 10.1007/s00410-012-0816-7

ORIGINAL PAPER

Geochronology and geochemistry of Cenozoic basalts from eastern Guangdong, SE China: constraints on the lithosphere evolution beneath the northern margin of the South China Sea

Xiao-Long Huang · Yaoling Niu · Yi-Gang Xu · Jin-Long Ma · Hua-Ning Qiu · Jun-Wei Zhong

Received: 7 March 2012 / Accepted: 21 September 2012 / Published online: 4 October 2012

Abstract The ^{40}Ar–^{39}Ar dating reveals three episodes of basaltic volcanism in eastern Guangdong of SE China since the late Eocene (i.e., 35.5, ~20 and 6.6 Ma). The Miocene alkali olivine basalts (~20 and 6.6 Ma) have OIB-like trace element characteristics, which is coupled with low $(^{87}Sr/^{86}Sr)_i$, high $\varepsilon_{Nd}(t)$, and high $\varepsilon_{Hf}(t)$. In contrast, the late Eocene basalts (35.5 Ma) have overall characteristics of "Island Arc" basalts with strong negative Ta–Nb–Ti anomalies in the primitive mantle-normalized multi-element diagram with high $(^{87}Sr/^{86}Sr)_i$, negative $\varepsilon_{Nd}(t)$, and relatively low $\varepsilon_{Hf}(t)$. All basalts have unexpectedly high $^{207}Pb/^{204}Pb$ and $^{208}Pb/^{204}Pb$, delineating a DUPAL signature in the sources. The late Eocene Arc-like basalts may reflect contributions of relict ancient metasomatized mantle lithosphere that melted as the result of extension-induced asthenospheric upwelling and heating, whereas the Miocene OIB-like basalts may represent partial melting of the asthenospheric mantle beneath the thickened lithosphere. We propose that the Cenozoic basaltic volcanism in eastern Guangdong records an overall lithospheric thickening process beneath SE China, that is, a continental rift system from its maximum extension in the late Eocene to its waning in the Miocene. This interpretation is consistent with the evolution of the South China Sea, whose origin is most consistent with the development of a passive continental margin. The seafloor spreading of the South China Sea during ~ 32–16 Ma may not result from the effect of the "Hainan" mantle plume, but rather played a positive role in allowing the mantle plume to express on the surface.

Keywords Lithospheric mantle · Asthenospheric mantle · Passive continental margin · Basalt · South China Sea

Communicated by J. Hoefs.

Electronic supplementary material The online version of this article (doi:10.1007/s00410-012-0816-7) contains supplementary material, which is available to authorized users.

X.-L. Huang (✉) · Y.-G. Xu · J.-L. Ma · H.-N. Qiu · J.-W. Zhong
State Key Laboratory of Isotope Geochemistry, Guangzhou Institute of Geochemistry, Chinese Academy of Sciences, Guangzhou 510640, China
e-mail: xlhuang@gig.ac.cn

Y. Niu
School of Earth Sciences, Lanzhou University, Lanzhou 730000, China

Y. Niu
Department of Earth Sciences, Durham University, Durham DH1 3LE, UK

J.-W. Zhong
Faculty of Land Resource Engineering, Kunming University of Science and Technology, Kunming 650093, China

Introduction

Basaltic volcanism on land is commonly thought to be associated with zones of continental rifting (Wilson 1989; Windley 1995). The controversy exists as to whether such rifting is developed along pre-existing zones of lithosphere weakness facilitated by dynamic mantle upwelling or simply results from lithospheric extension (Spohn and Schubert 1982).

The Cenozoic basaltic rocks of SE China, as part of the eastern China volcanic belts, are associated closely with major regional faults (Fig. 1) (e.g., Chung et al. 1994, 1997; Liu et al. 1994; Qi et al. 1994; Zou et al. 2000; Ho et al. 2003), which have been interpreted as genetically related to the opening of the South China Sea (SCS)

(Chung et al. 1994, 1997; Xu et al. 2002). However, the Cenozoic volcanism in South China was documented to show two distinct episodes (before 40 and after 16 Ma) with rare volcanism in between (Zhu and Wang 1989; Zhu et al. 2004; Ho et al. 2003). For this reason, the petrogenesis of these Cenozoic basalts would be unrelated to the opening of the SCS, which began at ~32 Ma with seafloor spreading ended at ~16 Ma (Briais et al. 1993). As a result, it remains unknown on the origin of the fault systems and related basaltic volcanism in South China. Several models have been proposed to explain the Cenozoic tectonomagmatic history in South China, including mantle plume origin (Deng et al. 2004; Xiao et al. 2004; Zhou et al. 2009), effects of Indian Ocean spreading (Zhu et al. 2004) and lithosphere extension (Chung et al. 1994, 1997). In addition, Ho et al. (2003) suggested that much of the late Cenozoic intraplate magmatism surrounding the SCS margins may be related to the migration of the SCS seafloor spreading center since the mid-Miocene. As almost all the late Cenozoic basaltic volcanism occurred following the cessation of the SCS seafloor spreading (<16 Ma), however, it is unclear how the magmatism in the region could have suddenly migrated from the SCS seafloor spreading center to the surrounding margins of the SCS.

We present here a new set of geochemical data on basalts from eastern Guangdong of SE China (also northern margin of the SCS) (Fig. 1a), including ^{40}Ar–^{39}Ar geochronology and Sr–Nd–Pb–Hf isotopes, to elucidate the magma source compositional evolution before the seafloor spreading of the SCS, during its active spreading (~32–16 Ma) (Briais et al. 1993) and after the cessation of the spreading. The study shows an overall lithospheric thickening process beneath SE China from the late Eocene to late Miocene, recording the tectonic evolution of continental rifting at a passive continental margin.

Geological setting and sample description

It is generally accepted that the Cenozoic volcanism in southeastern China can be divided into three NE–SW trending volcanic belts from east to west, that is, outer, middle, and inner belts (Chung et al. 1994; Qi et al. 1994; Zou et al. 2000) associated, respectively, with three lithospheric faults (Fig. 1). The Early Tertiary (38–64 Ma) volcanic rocks were restricted at the basins in the Central and Western Guangdong province, which were controlled by the NE–SW trending faults (Zhu et al. 2004). The Miocene to Pliocene (after 16 Ma, dominantly after 6 Ma) basalts were throughout the SE China (Zhu et al. 2004; Ho et al. 2003). Only a few basalt pipes have been found in eastern Guangdong province, Zhejiang Inner volcanic belt, and the northern part of the Hainan Island, likely formed during 34.3–16.3 Ma (Ho et al. 2003). The Cenozoic volcanism of eastern Guangdong (EGD) is at the southwestern end of the middle belt of Zhejiang-Fujian Cenozoic volcanic belts on land (Fig. 1a) and is dominated by alkali olivine basalts.

The basaltic samples were collected from Jilongshan (116°35′24″E, 23°27′04″N), Jiucaidi (116°04′05″E, 23°37′22″N), Puzhai (Puzhai116°09′56″E, 23°39′16″N), and Qilin (116°16′06″E, 23°22′40″N, location of borehole) (Fig. 1b). The Qilin pipe is a basaltic dyke with abundant mafic to ultramafic xenoliths dominated by spinel lherzolite with minor spinel harzburgite, spinel-garnet pyroxenite and granulite. The Qilin basalts, collected from a borehole, are porphyric (phenocrysts < 5 vol. %) with the groundmass composed of fine-grained plagioclase, clinopyroxene, and Fe–Ti oxide minerals. The Qilin samples are all partially alteration. All phenocrysts, as pseudomorphs of euhedral pyroxene, are completely replaced by talc. Microlitic clinopyroxenes in the groundmass are partially altered into actinolite. However, microlitic plagioclase resists to alteration and shows clear twins. Other three volcanic pipes (Jilongshan, Jiucaidi and Puzhai) are mostly basaltic rocks with few small spinel lherzolite xenoliths. The basaltic samples from Jilongshan, Jiucaidi, and Puzhai are all porphyritic with 10–15 vol. % phenocrysts dominated by olivine and clinopyroxene with minor orthopyroxene. The groundmass is mainly composed of fine-grained plagioclase, clinopyroxene, olivine, and Fe–Ti oxide minerals. The basalts from Puzhai and Jiucaidi are similar in petrography. The relatively larger (0.5–1 mm in size) olivine phenocrysts are all anhedral and always disintegrated along the rims or cracks. The relatively smaller (0.1–0.5 mm) olivine phenocrysts are both euhedral and anhedral. Orthopyroxene occurs as anhedral phenocrysts (0.1–0.3 mm) rimmed with reaction zones characterized by radially arranged fine-grained olivine and clinopyroxene. Clinopyroxene appears as euhedral or sub-euhedral phenocrysts (0.1–0.4 mm) and micro-phenocrysts (0.05–0.1 mm). In some samples, anhedral olivine, clinopyroxene, and orthopyroxene form crystal aggregates. The kink bands in olivine and the reaction zones in orthopyroxene of the aggregates are the same as those of isolated anhedral phenocrysts, suggesting their lithospheric mantle origin.

Analytical methods

Samples were sawed into slabs and the central parts were used for bulk rock analyses. The rocks were crushed into small size (<0.5 cm in diameter) before further cleaned with deionized water in an ultrasonic bath and powdered in a corundum mill. The samples were prepared as glass discs

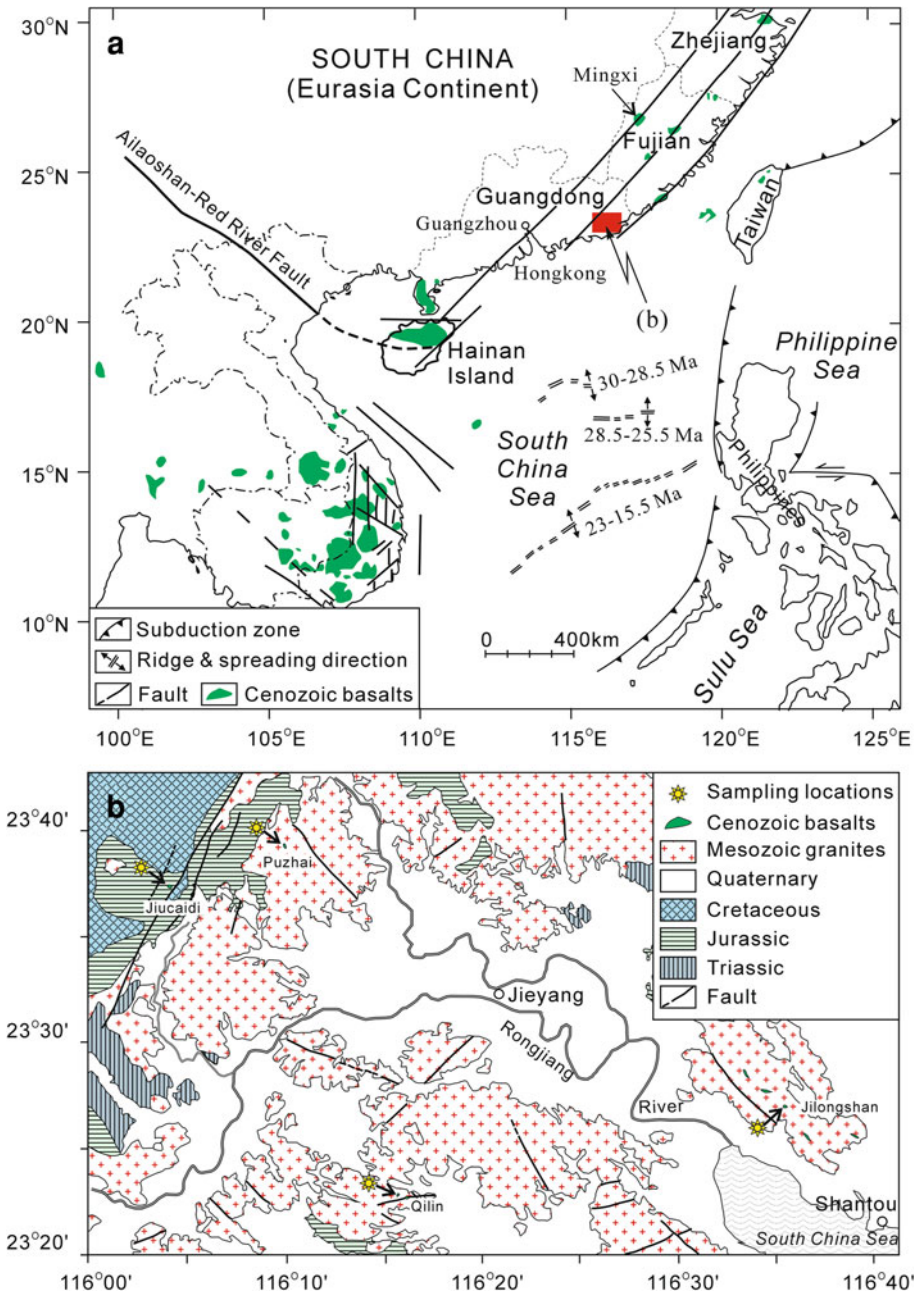

Fig. 1 **a** Sketch map of the tectonic framework South China in a broad regional context (after Xu et al. 2002; Sun et al. 2009). **b** Simplified geological map of eastern Guangdong province, illustrating the distribution of the sample locations (modified after the Shantou geological map of 1/200,000 scale; BGMR 1974)

using a Rigaku desktop fusion machine. Bulk rock major element oxides were analyzed using a Rigaku RIX 2000 X-ray fluorescence spectrometer (XRF) at the State Key Laboratory of Isotope Geochemistry, Guangzhou Institute of Geochemistry, Chinese Academy of Sciences (GIG-CAS). Calibration lines used in quantification were produced by bivariate regression of data from 36 reference materials encompassing a wide range of silicate compositions (Li et al. 2005). Calibrations incorporated matrix corrections based on the empirical Traill-Lachance procedure, and analytical uncertainties are better than 5 % (Supplemental Table 1).

Trace elements were analyzed using inductively coupled plasma mass spectrometry (ICP-MS) after acid digestion of samples in high-pressure Teflon vessels at the State Key Laboratory of Isotope Geochemistry, GIG-CAS. The US Geological Survey and Chinese National standards GSR-1, GSR-2, GSR-3, G-2, W-2, BT142, AGV-2, MRG-1, and ROA-1 were chosen for calibrating element concentrations of measured samples. Analytical precision of REE and other incompatible elements is typically 1–5 % (Supplemental Table 2).

Sr–Nd isotopic ratios were measured on a subset of whole rock samples using a Micromass Isoprobe Multi-Collector

Inductively Coupled Plasma Mass Spectrometry (MC-ICPMS) at the State Key Laboratory of Isotope Geochemistry, GIG-CAS following the procedure of Wei et al. (2002). Reference standards were analyzed along with samples and give $^{87}Sr/^{86}Sr = 0.710243 \pm 14$ (2σ, the last 2 digits) for NBS987 and $^{143}Nd/^{144}Nd = 0.512124 \pm 11$ (2σ) for Shin Etsu JNdi-1 (0.512115 ± 7; Tannaka et al. 2000).

For Pb isotope measurements, 100 mg of rock powder was weighed into a Teflon cup and dissolved in a HNO_3 + HF mixture at 140 °C for 72 h. The solution was evaporated to dryness, then added with 2 mL concentrated HNO_3, and kept on a hot plate at 140 °C for 24 h. It was evaporated to dryness again, subsequently added with 2 mL 6 M HCl, and kept on a hot plate at 140 °C for another 24 h. It was finally dissolved in 0.8 M HBr solution in preparation for Pb purification. Pb was separated and purified by conventional anion exchange techniques (AG1X8, 200–400 resin) with dilute HBr as eluant. The total procedural blank is less than 0.4 ng. Pb isotopic ratios were measured with a Nu Plasma high resolution multi-collector mass spectrometer (HR MC-ICPMS) at Xiamen University, China, using an exponential correction relative to $^{205}Tl/^{203}Tl = 2.3871$. The detail analytical procedures are similar to those described by Baker and Waight (2002). During the period of analysis, repeated analyses of international standard NIST SRM981 yielded $^{206}Pb/^{204}Pb = 16.9317 \pm 2$ (2σ), $^{207}Pb/^{204}Pb = 15.4805 \pm 6$ (2σ), and $^{208}Pb/^{204}Pb = 36.6632 \pm 4$ (2σ).

For Hf isotope analysis, the mixture of about 100 mg rock powder and 200 mg $Li_2B_4O_7$ was fused in a Pt–Au alloy crucible at 1,200 °C for 15 min in a high-frequency furnace. The quenched piece of alkali glass was dissolved in 2 mol/L HCl. Hf fraction was separated by using a modified single-column Ln extraction chromatography method. Hf isotopes were determined using HR MC-ICPMS at Xiamen University, China. The measured $^{176}Hf/^{177}Hf$ ratios were normalized to $^{179}Hf/^{177}Hf = 0.7325$, and the reported $^{176}Hf/^{177}Hf$ ratios were further adjusted relative to the standard JMC-475 of 0.282160. During the course of this study, basalt standards BHVO-2 and JB-3 yield $^{176}Hf/^{177}Hf$ ratios of 0.283090 ± 4 ($2\sigma_n$, $n = 6$) and 0.283234 ± 2 ($2\sigma_n$, $n = 6$), respectively.

For $^{40}Ar/^{39}Ar$ dating, the rock was sawed into slabs and the central part was used. After crushed into 40–60 mesh size in a steel mortar with all phenocrysts removed under a binocular, the sample was cleaned with acetone followed by further cleaning with deionized water in an ultrasonic bath. The cleaned sample was then dried at ~100 °C. Each sample was wrapped in aluminum foil and sealed in a quartz ampoule that was evacuated afterward before being irradiated for 90 h in the Mianyang reactor (Sichuan, China). The *J*-values for the samples were determined by ZBH-2506 Biotite (132 Ma) flux monitors. In order to obtain *J*-values for the samples, the monitor ZBH-2506 was packed between every four samples in quartz tubes, each tube containing 4 packets of ZBH-2506. Based on the *J*-values and the positions of ZBH-2506 in the sample tube, a regression line was obtained for each sample tube, and then the *J*-values of the samples were calculated by interpolation from the regression line. The *J*-value uncertainty of 0.15 % (1σ) was considered in the reported ages. The $^{40}Ar/^{39}Ar$ dating was carried out at the GIG-CAS using a GV5400 mass spectrometer. Argon gas was extracted from the sample by step-heating (50 s per step) using a MIR10 CO_2 continuing laser. The background of the sample hold is lower than 2 mV pre-experiment and 4–6 mV during experiment (after 5 min vacuumize), while the signal of the sample is mostly controlled within the range of 40–200 mV. The ArArCALC program (v.2.2; Koppers 2002) was used for data reduction and age calculation.

Results

$^{39}Ar/^{40}Ar$ dating

Samples from the four locations of eastern Guangdong were dated with the $^{40}Ar/^{39}Ar$ method (Table 1). The age spectrums of all $^{40}Ar/^{39}Ar$ dating results are shown in Fig. 2. The plateau age of Qilin basalt is 35.5 ± 0.4 Ma (cumulative ^{39}Ar released >70 %; Fig. 2a) and that of Jilongshan basalt is 6.64 ± 0.07 Ma (cumulative ^{39}Ar released >80 %; Fig. 2b). Puzhai and Jiucaidi basalts have very close plateau ages of 20.2 ± 0.1 Ma (cumulative ^{39}Ar released >90 %; Fig. 2c) and 20.8 ± 0.1 Ma (cumulative ^{39}Ar released >90 %; Fig. 2d), respectively.

Major and trace elements

All the analyzed samples show a narrow compositional range with 44.4 wt % to 48.7 wt % SiO_2 (Supplemental Table 3). The total alkalis ($Na_2O + K_2O$) vary in the range of 4.6–6.5 wt % (Supplemental Table 3). The Na_2O/K_2O ratios of the Jilongshan, Jiucadai, and Puzhai basalts are more than unity, indicating their alkali-rich and high-sodium nature, while the Qilin basalts have relatively high K_2O (2.76–3.29 wt %), low Na_2O (1.74–2.06 wt %), and low Na_2O/K_2O ratios of 0.53–0.75. Following Le Maitre (1989), the Jiucaidi, Puzhai, and Jilongshan samples are trachybasalt, alkali basalts, or basanite, while the Qilin samples are trachybasalt or basaltic trachyandesite (Fig. 3a). The Qilin samples have relatively higher $Mg^{\#}$ (> 0.70), SiO_2 (47.7–48.7 wt %), Al_2O_3 (16.2–16.8 wt %), but lower Fe_2O_3 (8.9–10.0 wt %), TiO_2 (1.34–1.37 wt %), Cr (124–142 ppm) and Ni (80–96 ppm) than samples from

Table 1 $^{40}Ar/^{39}Ar$ dating of the eastern Guangdong Cenozoic basalts

Incremental heating		$^{36}Ar(a)$	$^{38}Ar(cl)$	$^{39}Ar(k)$	$^{40}Ar(r)$	Age ± 2σ (Ma)	$^{40}Ar(r)$	$^{39}Ar(k)$
Steps	Laser (%)						(%)	(%)
QILIN-1 (Whole Rock)		T1 = 35.51 ± 0.36 Ma; T2 = 34.67 ± 0.18 Ma; T3 = 36.04 ± 0.69 Ma; T4 = 35.78 ± 0.78 Ma						
05M2114B	3.0	0.007	0.004	4.787	7.023	28.88 ± 0.80	77.99	2.91
05M2114C	4.0	0.018	0.002	14.828	23.163	30.74 ± 0.51	81.26	9.00
05M2114D	4.5	0.007	0.000	15.680	25.964	32.57 ± 0.53	91.96	9.52
05M2114E	5.0	0.007	0.000	13.251	23.502	34.86 ± 0.61	91.59	8.04
05M2114G	5.5	0.000	0.000	11.399	20.249	34.92 ± 0.36	99.67	6.92
05M2114H	6.2	0.002	0.000	13.022	23.481	35.44 ± 0.51	97.01	7.90
05M2114I	7.0	0.006	0.000	14.144	25.195	35.01 ± 0.42	92.92	8.59
05M2114 J	8.0	0.005	0.005	16.763	30.168	35.37 ± 0.41	94.75	10.18
05M2114L	9.0	0.002	0.009	13.590	24.857	35.94 ± 0.48	97.83	8.25
05M2114 M	10.5	0.002	0.009	13.276	24.367	36.07 ± 0.51	97.90	8.06
05M2114 N	12.5	0.004	0.010	13.143	24.028	35.93 ± 0.53	95.17	7.98
05M2114O	15.0	0.003	0.005	9.547	17.656	36.34 ± 0.69	94.89	5.80
05M2114Q	20.0	0.001	0.002	6.045	10.953	35.61 ± 0.76	96.96	3.67
05M2114R	50.0	0.002	0.003	4.779	8.965	36.86 ± 0.71	92.41	2.90
05M2114S	100.0	0.002	0.000	0.482	0.979	39.86 ± 6.81	58.61	0.29
JCD-9 (Whole Rock)		T1 = 20.77 ± 0.14 Ma; T2 = 20.79 ± 0.16 Ma; T3 = 20.50 ± 0.38 Ma; T4 = 20.50 ± 0.38 Ma						
05M2116B	3.0	0.010	0.053	5.592	5.668	19.70 ± 0.64	66.32	4.63
05M2116C	4.0	0.015	0.136	16.661	17.851	20.82 ± 0.30	79.34	13.80
05M2116D	4.5	0.009	0.082	12.686	13.574	20.80 ± 0.40	83.70	10.51
05M2116E	5.0	0.005	0.051	9.336	9.999	20.82 ± 0.38	85.94	7.73
05M2116G	6.0	0.006	0.046	11.848	12.714	20.86 ± 0.33	86.54	9.81
05M2116H	7.0	0.004	0.021	10.123	10.680	20.51 ± 0.36	88.82	8.38
05M2116I	8.5	0.006	0.016	10.334	10.963	20.62 ± 0.38	85.79	8.56
05M2116 K	10.5	0.003	0.006	3.617	3.839	20.63 ± 0.59	81.22	3.00
05M2116L	16.0	0.005	0.011	6.506	6.946	20.75 ± 0.62	81.50	5.39
05M2116 M	25.0	0.017	0.021	12.129	12.787	20.49 ± 0.63	71.78	10.05
05M2116 N	35.0	0.015	0.019	11.714	12.821	21.27 ± 0.66	73.84	9.70
05M2116P	45.0	0.011	0.011	7.204	7.875	21.25 ± 0.75	69.93	5.97
05M2116Q	60.0	0.008	0.006	2.980	3.416	22.28 ± 1.29	57.85	2.47
PUZ-9 (Whole Rock)		T1 = 20.24 ± 0.13 Ma; T2 = 20.25 ± 0.14 Ma; T3 = 20.35 ± 0.87 Ma; T4 = 20.36 ± 0.86 Ma						
05M2115B	3.0	0.004	0.042	3.840	3.944	20.13 ± 0.98	78.24	3.44
05 M2115C	4.0	0.008	0.161	16.128	16.796	20.41 ± 0.28	86.62	14.43
05M2115D	5.0	0.009	0.168	18.471	19.106	20.27 ± 0.30	86.97	16.52
05M2115E	6.0	0.010	0.166	17.292	17.760	20.13 ± 0.23	85.81	15.47
05M2115G	7.0	0.007	0.133	14.430	14.959	20.31 ± 0.31	87.71	12.91
05M2115H	8.0	0.007	0.110	12.809	13.168	20.15 ± 0.34	85.94	11.46
05M2115I	9.5	0.006	0.063	9.012	9.295	20.21 ± 0.50	84.48	8.06
05M2115 J	12.0	0.005	0.046	7.012	7.271	20.32 ± 0.67	83.26	6.27
05 M2115L	15.0	0.005	0.052	8.222	8.494	20.25 ± 0.55	84.78	7.35
05M2115M	19.0	0.004	0.020	4.576	4.736	20.28 ± 0.86	81.59	4.09
JLS-4 (Whole Rock)		T1 = 6.64 ± 0.07 Ma; T2 = 7.04 ± 0.10 Ma; T3 = 6.62 ± 0.15 Ma; T4 = 6.61 ± 0.15 Ma						
05M2117A	2.5	0.003	0.004	0.537	0.213	7.69 ± 3.06	18.80	0.32
05M2117B	3.0	0.003	0.027	2.459	0.870	6.87 ± 0.80	46.32	1.44
05M2117D	3.5	0.003	0.051	5.564	1.847	6.45 ± 0.48	66.40	3.26
05M2117E	4.2	0.006	0.078	12.714	4.359	6.66 ± 0.23	69.12	7.45
05M2117F	4.7	0.005	0.060	13.342	4.454	6.48 ± 0.36	74.95	7.82

Table 1 continued

Incremental heating		^{36}Ar(a)	^{38}Ar(cl)	^{39}Ar(k)	^{40}Ar(r)	Age ± 2σ (Ma)	^{40}Ar(r)	^{39}Ar(k)
Steps	Laser (%)						(%)	(%)
05M2117G	5.5	0.004	0.063	18.231	6.183	6.58 ± 0.22	81.46	10.69
05M2117I	6.5	0.003	0.062	19.144	6.535	6.63 ± 0.23	86.35	11.22
05M2117 J	8.5	0.004	0.067	28.907	9.880	6.63 ± 0.20	88.58	16.95
05M2117 K	10.5	0.003	0.040	23.770	8.160	6.66 ± 0.20	89.32	13.94
05M2117L	13.5	0.000	0.007	5.141	1.767	6.67 ± 0.13	98.29	3.01
05M2117 N	16.0	0.002	0.007	4.679	1.570	6.51 ± 0.45	75.43	2.74
05M2117O	21.0	0.002	0.012	8.171	2.810	6.68 ± 0.42	80.31	4.79
05M2117P	31.0	0.008	0.033	18.099	8.600	9.22 ± 0.44	78.02	10.61
05M2117Q	45.0	0.006	0.020	9.799	4.572	9.05 ± 0.68	72.27	5.75

The argon isotopes are listed in volt: ^{36}Ar(a), air argon; ^{38}Ar(cl), Cl-derived nucleogenic ^{38}Ar; ^{39}Ar(k), K-derived nucleogenic ^{39}Ar; ^{40}Ar(r), nucleogenic ^{40}Ar

T1, weighted plateau age; T2, total fusion age; T3, normal isochron age; T4, inverse isochron age

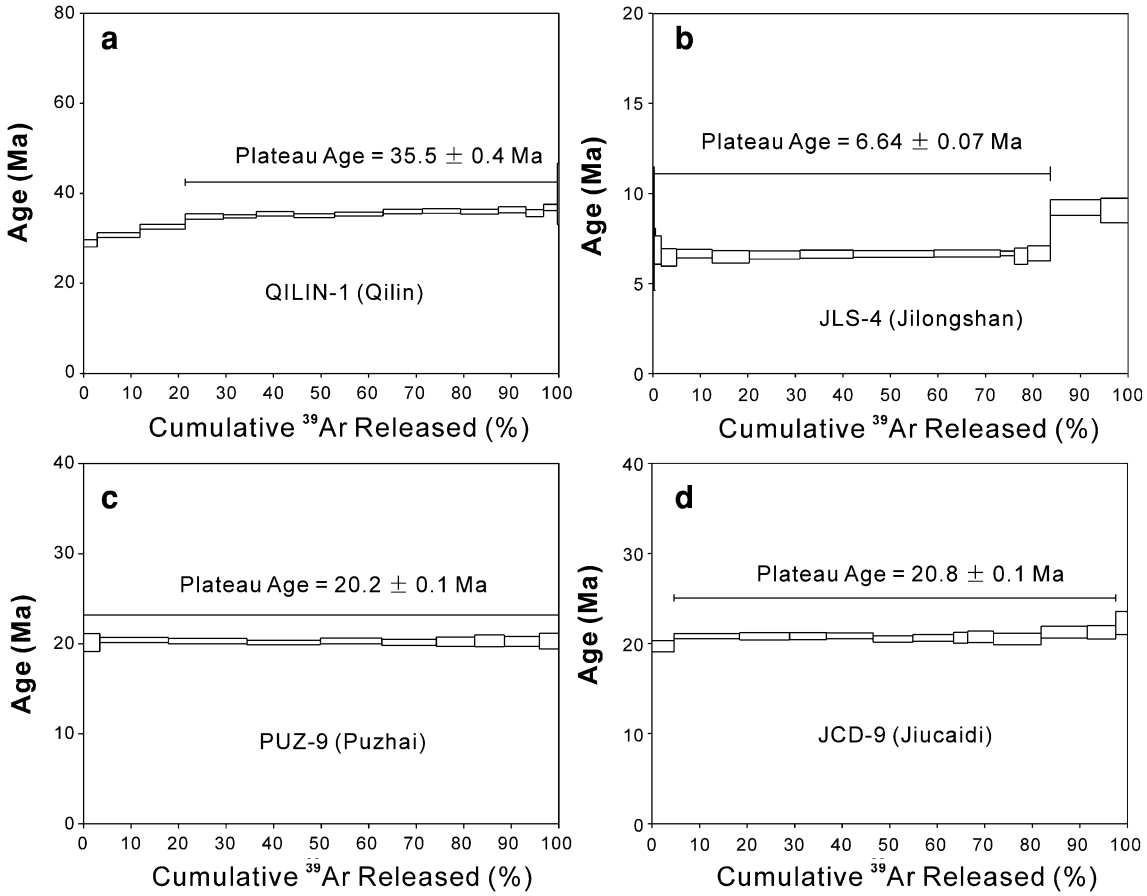

Fig. 2 Whole-rock ^{40}Ar/^{39}Ar plateau ages spectra for four representative samples

Jiucaidi, Puzhai, and Jilongshan ($Mg^{\#}$ = 0.59–0.67; Fe_2O_3 = 13.0–13.7 wt %; TiO_2 = 2.09–2.81 wt %) (Fig. 3; Supplemental Table 3). Taken all samples together, TiO_2 decrease with increasing $Mg^{\#}$ (Fig. 3b).

In chondrite-normalized rare earth element (REE) patterns (Fig. 4a), all samples are highly enriched in light REEs relative to heavy REEs ($[La/Yb]_N$ = 6.2–30.1). The Jiucaidi, Puzhai, and Jilongshan basalts show decreasing

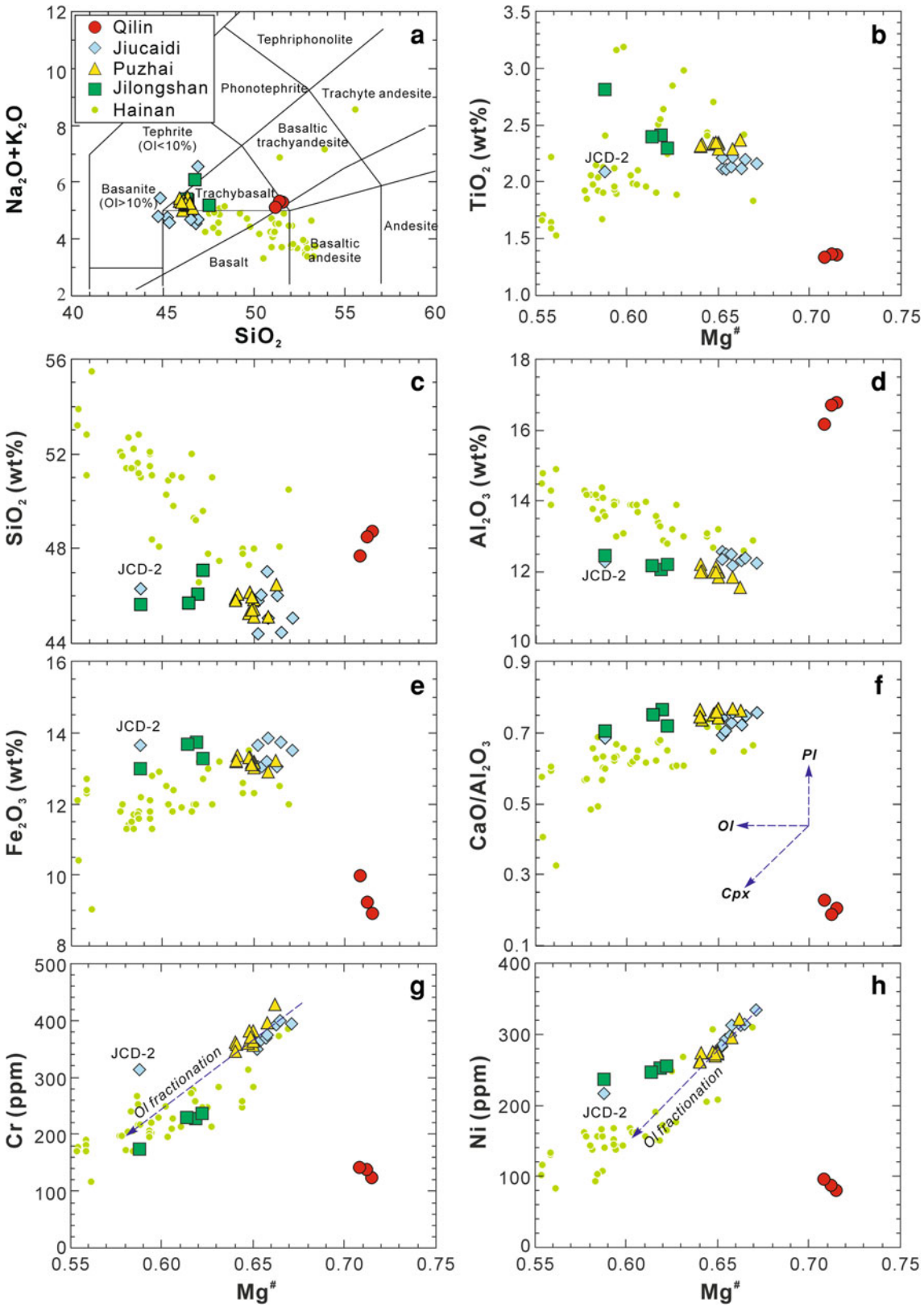

Fig. 3 **a** TAS diagram, the data had been volatile corrected (Le Maitre 1989); **b** TiO_2 vs. $Mg^{\#}$; **c** SiO_2 vs. $Mg^{\#}$; **d** Al_2O_3 vs. $Mg^{\#}$; **e** Fe_2O_3 vs. $Mg^{\#}$; **f** CaO/Al_2O_3 vs. $Mg^{\#}$; **g** Cr vs. $Mg^{\#}$ and **h** Ni vs. $Mg^{\#}$ for the eastern Guangdong Cenozoic basalts. The Hainan OIBs are from Wang et al. (2012)

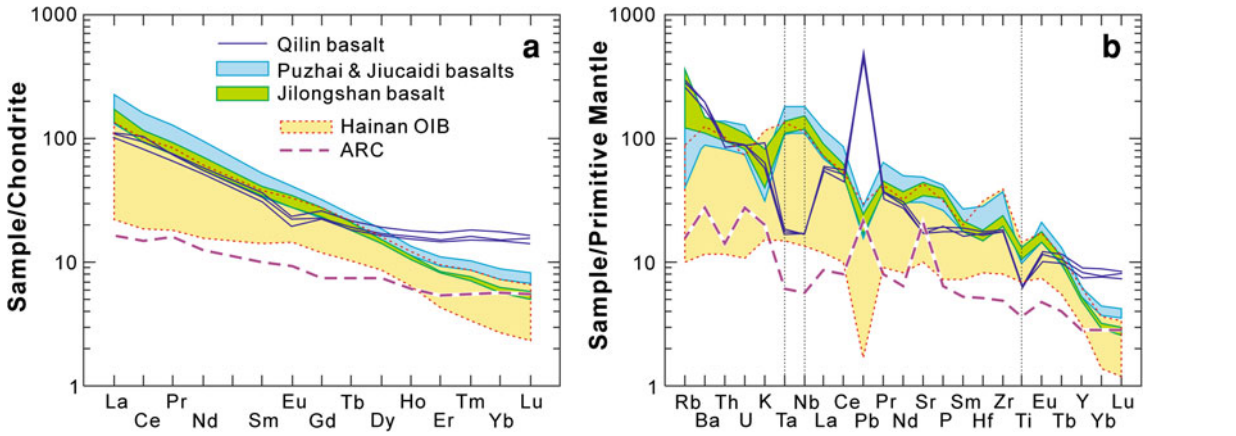

Fig. 4 **a** Chondrite-normalized REE patterns and **b** primitive mantle-normalized multi-element patterns of the eastern Guangdong Cenozoic basalts. Chondrite normalization values are from Taylor and McLennan (1985), PM normalization values are from Sun and McDonough (1989). The Hainan OIBs are from Wang et al. (2012), and ARC is average of Aleutian island arc basalt (Kelemen et al. 2003)

heavy REE patterns without an obvious negative Eu anomaly (Eu/Eu* = 0.94–1.00), while the Qilin basalts show flat heavy REE pattern with a moderate negative Eu anomaly (Eu/Eu* = 0.73–0.79) (Fig. 4a). These features are consistent with the petrography that the Jiucaidi, Puzhai, and Jilongshan basalts have liquidus phases (phenocrysts) of olivine + clinopyroxene without plagioclase, while plagioclase is the dominant liquidus phase (phenocryst) in the Qilin samples.

The alkali basalts from Jiucaidi, Puzhai, and Jilongshan are all enriched in incompatible trace elements with positive Nb–Ta anomalies ($[Nb/La]_N$ = 1.40–1.68; Supplemental Table 3) and obvious negative Pb and Ti anomalies (Fig. 4b) in the primitive mantle-normalized multi-element diagram, resembling present-day ocean island basalts (OIB). However, the Qilin basalts exhibit strong negative Ta–Nb–Ti anomalies ($[Nb/La]_N$ = 0.28–0.31) and a positive Pb anomaly (Fig. 4b). This pattern resembles that of the present-day "Island Arc" basalts, though at a high concentration level (Fig. 4b).

Sr–Nd–Hf-Pb isotopes

The Jiucaidi and Puzhai basalts show a very limited range in $^{143}Nd/^{144}Nd$ and $^{87}Sr/^{86}Sr$ ratios, uniform $\varepsilon_{Nd}(t)$ (+4.94 to +5.95; Table 2), low initial $^{87}Sr/^{86}Sr$ (0.7037–0.7038), and high initial $^{143}Nd/^{144}Nd$ (0.51287–0.51292). The Jilongshan basalts have slightly lower $\varepsilon_{Nd}(t)$ (+4.44 to +4.63) and higher initial $^{87}Sr/^{86}Sr$ ratios (~0.7039) than the Jiucaidi and Puzhai basalts (Table 2; Fig. 5a). The Qilin basalts have the lowest $\varepsilon_{Nd}(t)$ (−3.64 to −2.77) and highest initial $^{87}Sr/^{86}Sr$ (0.7075–0.7077) in the Cenozoic basalts of eastern Guangdong.

The Jiucaidi and Puzhai (~20 Ma) and Jilongshan (~6.5 Ma) samples have high $\varepsilon_{Hf}(t)$ values clustered around +8.1 to +9.6, whereas the Qilin (~35.5 Ma) samples have low $\varepsilon_{Hf}(t)$ values between +0.06 and +0.74 (Table 2). The Nd–Hf isotopic compositions for Jiucaidi, Puzhai, and Jilongshan samples are correlated and plot on the OIB array line (Chauvel et al. 2008), while the Qilin samples plot slightly above the array line (Fig. 5b). Following Chauvel et al. (2008), we calculate the $\Delta\varepsilon_{Hf}$ values (the difference in ε_{Hf} relative to the ε_{Nd}–ε_{Hf} mantle array, defined as $\Delta\varepsilon_{Hf} = \varepsilon_{Hf} - 1.59\varepsilon_{Nd} - 1.28$) to evaluate the degree of Nd–Hf decoupling of the EGD basalts (Table 2). The $\Delta\varepsilon_{Hf}$ values of the Jilongshan samples range from −0.67 to −0.04, those of the Jiucaidi and Puzhai samples are −1.60 to −0.09, all of which are within analytical errors. However, the Qilin samples have relatively high $\Delta\varepsilon_{Hf}$ values of 3.87–4.56 (Table 2), which is consistent with the Qilin basalts having elevated HREEs (i.e., higher Lu/Hf than the other basalt suites; Fig. 4b).

The samples all display unexpectedly high $^{207}Pb/^{204}Pb$ (15.579–15.656) and $^{208}Pb/^{204}Pb$ (38.893–38.949) in comparison with MORB-like $^{206}Pb/^{204}Pb$ (18.656–18.774) (Table 3). The Qilin samples have slightly higher $^{207}Pb/^{204}Pb$ but lower $^{208}Pb/^{204}Pb$ than the other samples (Fig. 5d, e). The initial radiogenic Pb isotope ratios of all the Cenozoic basalts of eastern Guangdong plot above the Northern Hemisphere reference line (NHRL; Hart 1984) (Fig. 5d, e). Similar Pb isotopic characteristics have been observed in the post-spreading seamount basalts from the SCS and other late Cenozoic basalts from Southeast China (Fig. 5d, e) and described as DUPAL anomaly (Tu et al. 1991, 1992; Flower et al. 1992; Zhang et al. 1996; Zou et al. 2000).

Table 2 Sr, Nd and Hf isotope data for the eastern Guangdong Cenozoic basalts

Samples	$^{87}Rb/^{86}Sr$	$^{87}Sr/^{86}Sr$ ($\pm 2\sigma$)	$(^{87}Sr/^{86}Sr)_i$	$^{147}Sm/^{144}Nd$	$^{143}Nd/^{144}Nd$ ($\pm 2\sigma$)	$(^{143}Nd/^{144}Nd)_i$	T_{DM} (Ma)	$\varepsilon_{Nd}(t)$	$^{176}Lu/^{177}Hf$	$^{176}Hf/^{177}Hf$ ($\pm 2\sigma$)	$(^{176}Hf/^{177}Hf)_i$	$\varepsilon_{Hf}(t)$	$T_{DM\text{-}Hf}$ (Ma)	$\Delta\varepsilon_{Hf}$
JCD-1	0.223	0.703755 ± 14	0.703692	0.110	0.512932 ± 6	0.512917	324	5.95	0.00615	0.283047 ± 2	0.283047	9.64	335	−1.10
JCD-2	0.264	0.703779 ± 14	0.703704	0.107	0.512883 ± 9	0.512869	385	5.00	0.00418	0.283033 ± 2	0.283033	9.15	339	−0.09
JCD-8	0.267	0.703731 ± 14	0.703655	0.111	0.512928 ± 11	0.512914	332	5.88	0.00616	0.283030 ± 2	0.283030	9.03	364	−1.60
JCD-9	0.205	0.703895 ± 17	0.703837	0.112	0.512924 ± 9	0.512909	341	5.80	0.00635	0.283041 ± 2	0.283041	9.40	349	−1.10
PUZ-2	0.130	0.703793 ± 14	0.703756	0.114	0.512902 ± 6	0.512887	380	5.36	0.00708	0.283020 ± 2	0.283020	8.66	392	−1.13
PUZ-3	0.121	0.703829 ± 14	0.703794	0.112	0.512915 ± 9	0.512900	356	5.62	0.00681	0.283023 ± 2	0.283023	8.75	384	−1.45
PUZ-5	0.197	0.703894 ± 14	0.703838	0.113	0.512906 ± 9	0.512891	370	5.45	0.00733	0.283028 ± 2	0.283028	8.92	382	−1.01
PUZ-9	0.138	0.703866 ± 14	0.703826	0.112	0.512880 ± 8	0.512866	406	4.94	0.00691	0.283019 ± 2	0.283019	8.62	392	−0.51
PUZ-13	0.095	0.703733 ± 14	0.703706	0.113	0.512893 ± 9	0.512878	393	5.19						
JLS-1	0.323	0.703924 ± 13	0.703897	0.119	0.512863 ± 9	0.512858	465	4.44	0.00648	0.282999 ± 3	0.282999	7.67	420	−0.67
JLS-4	0.341	0.703988 ± 6	0.703959	0.119	0.512864 ± 5	0.512860	461	4.48	0.00645	0.283018 ± 2	0.283018	8.36	387	−0.04
JLS-9	0.305	0.703954 ± 13	0.703928	0.121	0.512872 ± 8	0.512867	460	4.63	0.00657	0.283017 ± 2	0.283017	8.31	391	−0.32
JLS-10	0.708	0.703963 ± 13	0.703902	0.116	0.512869 ± 9	0.512865	441	4.57	0.00470	0.283009 ± 2	0.283009	8.05	381	−0.49
QILIN-1	1.377	0.708162 ± 17	0.707468	0.121	0.512434 ± 8	0.512406	1175	−3.64	0.01620	0.282775 ± 3	0.282775	0.06	1134	4.56
QILIN-3	1.443	0.708285 ± 13	0.707557	0.117	0.512451 ± 9	0.512424	1101	−3.29	0.01441	0.282784 ± 2	0.282784	0.41	1031	4.36
QL07-1	1.318	0.708392 ± 14	0.707727	0.120	0.512478 ± 8	0.512450	1097	−2.77	0.01663	0.282795 ± 3	0.282795	0.74	1109	3.87
MXG	0.186	0.710817 ± 16	0.710722	0.094	0.512094 ± 8	0.512072	1345	−10.14						

MXG: felsic granulite xenolith in the Mingxi Cenozoic basalt

^{87} Rb/^{86}Sr, ^{147}Sm/^{144}Nd, and ^{176}Lu/^{177}Hf are calculated using whole-rock Rb, Sr, Sm, Nd, Lu and Hf contents in Supplemental Table 3

In the calculation of $\varepsilon_{Nd}(t)$ and T_{DM}, $(^{143}Nd/^{144}Nd)_{CHUR} = 0.512638$, $(^{147}Sm/^{144}Nd)_{CHUR} = 0.1967$, $(^{143}Nd/^{144}Nd)_{DM} = 0.51315$, $(^{147}Sm/^{144}Nd)_{DM} = 0.2136$. t = 36 Ma (Qilin basalt and Mingxi granulite xenolith), 20 Ma (Puzhai and Jiucaidi basalts), 6.6 Ma (Jilongshan basalt)

In the calculation of $\varepsilon_{Hf}(t)$ and $T_{DM\text{-}Hf}$, $(^{176}Hf/^{177}Hf)_{CHUR} = 0.282785$, $(^{176}Lu/^{177}Hf)_{CHUR} = 0.0336$ (Bouvier et al. 2008), $(^{176}Lu/^{177}Hf)_{DM} = 0.0384$, $(^{176}Hf/^{177}Hf)_{DM} = 0.28325$ (Griffin et al. 2000), $\lambda(^{176}Lu) = 1.867 \times 10^{-11}$ year^{-1} (Söderlund et al. 2004)

$\Delta\varepsilon_{Hf} = \varepsilon_{Hf} - 1.59\varepsilon_{Nd} - 1.28$ (Chauvel et al. 2008)

Table 3 Pb isotope data of the eastern Guangdong Cenozoic basalts

Samples	$^{206}Pb/^{204}Pb$	$^{207}Pb/^{204}Pb$	$^{208}Pb/^{204}Pb$	μ	k	$(^{206}Pb/^{204}Pb)_i$	$(^{207}Pb/^{204}Pb)_i$	$(^{208}Pb/^{204}Pb)_i$	Δ7/4	Δ8/4
JCD-1	18.7408 ± 20	15.5845 ± 12	38.8928 ± 34	32.3	148	18.640	15.580	38.746	6.8	58.3
JCD-2	18.7737 ± 20	15.5791 ± 13	38.9137 ± 41	33.6	150	18.669	15.574	38.765	6.0	56.7
JLS-1	18.6880 ± 19	15.6068 ± 12	38.9339 ± 35	37.0	177	18.654	15.605	38.881	9.2	70.2
JLS-9	18.6561 ± 16	15.6063 ± 10	38.8961 ± 22	33.0	161	18.625	15.605	38.848	9.5	70.3
PUZ-2	18.7367 ± 7	15.6034 ± 7	38.9269 ± 17	31.7	143	18.638	15.599	38.785	8.7	62.4
PUZ-5	18.7652 ± 16	15.6012 ± 9	38.9490 ± 27	31.3	135	18.668	15.597	38.815	8.2	61.9
QILIN-1	18.6680 ± 6	15.6559 ± 6	38.8036 ± 15	1.3	5.8	18.661	15.656	38.793	14.2	60.5
QILIN-3	18.6640 ± 4	15.6521 ± 4	38.7911 ± 11	1.3	5.2	18.657	15.652	38.782	13.8	59.9
QL07-1	18.6660 ± 7	15.6515 ± 8	38.7880 ± 18	1.5	6.6	18.658	15.651	38.776	13.8	59.2
MXG	17.9941 ± 8	15.6075 ± 9	38.6299 ± 20	1.6	2.6	17.985	15.607	38.625	16.7	125.4

MXG: felsic granulite xenolith in the Mingxi Cenozoic basalt

$\Delta 7/4 = [(^{207}Pb/^{204}Pb)_i - (^{207}Pb/^{204}Pb)_{NHRL}] \times 100$; $\Delta 8/4 = [(^{208}Pb/^{204}Pb)_i - (^{208}Pb/^{204}Pb)_{NHRL}] \times 100$;
$(^{207}Pb/^{204}Pb)_{NHRL} = 0.1084 \times (^{206}Pb/^{204}Pb)_i + 13.491$; $(^{208}Pb/^{204}Pb)_{NHRL} = 1.209 \times (^{206}Pb/^{204}Pb)_i + 15.627$ (Hart 1984)

Initial Pb isotope ratios are calculated using whole-rock U, Th, and Pb contents in Supplemental Table 3. t = 36 Ma (Qilin basalt and Mingxi granulite xenolith), 20 Ma (Puzhai and Jiucaidi basalts), 6.6 Ma (Jilongshan basalt)

Discussion

Mantle sources constraints from basalt geochemistry

Cenozoic basaltic rocks of SE China are traditionally regarded as relating to the seafloor spreading of the SCS (Chung et al. 1994, 1997; Xu et al. 2002), which began at ~32 Ma and ended at ~16 Ma (Briais et al. 1993). The Early Tertiary volcanic rocks, including the early andesite-rhyolite (64–56 Ma) and the later basalt-trachyte (38–56 Ma), were restricted at the basins (Chung et al. 1997; Zhu et al. 2004; Zhou et al. 2009). The Miocene to Pliocene (after 16 Ma, dominantly after 6 Ma) basalts were throughout the SE China (Zhu et al. 2004; Ho et al. 2003), but only several basalt pipes likely formed during 34.3–16.3 Ma (Ho et al. 2003). So, it is a rare opportunity to reveal the possible mantle source evolution in the region in terms of the SCS seafloor spreading history. The three episodes of basaltic volcanism (35.5, ~20 and 6.6 Ma) revealed by $^{40}Ar/^{39}Ar$ dating in the eastern Guangdong area indicate that the Cenozoic volcanism actually took place prior to, during and after the seafloor spreading of the SCS (32–16 Ma; Briais et al. 1993) in the same region. Thus, the Sr–Nd–Hf–Pb isotopes and trace element systematics of these basalts can be used in combination to discuss the nature of the basaltic magmatism and associated mantle sources beneath the continental margin of SE China in the context of the SCS evolution.

Miocene OIB-type basalts (~20 and 6.6 Ma)

Crustal contamination is inevitable for mantle-derived melts during their ascent through, and evolution within, magma chambers under the continental environment. Nevertheless, the Miocene alkali basalts from Jiucaidi, Puzhai, and Jilongshan all display OIB-like patterns on the primitive mantle-normalized multi-element diagram (Fig. 4b), which indicates rather insignificant crustal contamination in their petrogenesis. Any significant crustal assimilation can also be ruled out because of the very different Sr–Nd–Pb isotopes between the basalts and the lower crustal xenoliths (e.g., MXG) (Fig. 5). According to the correlations of CaO/Al_2O_3, Cr and Ni vs $Mg^{\#}$, the compositional variations of EGD Miocene basalts must be attributed to fractional crystallization of dominant olivine (Fig. 3f, g, h). Thus, the characteristics of isotopes and incompatible trace elements of the EGD Miocene basalts may reflect those of the magma source.

All the EGD Miocene OIB-type basalts have radiogenic $^{207}Pb/^{204}Pb$ and $^{208}Pb/^{204}Pb$ isotope ratios that plot above the Northern Hemisphere Pb reference line (NHRL; Hart 1984) (Fig. 5d, e). Similar Pb isotopic features had been observed in the post-spreading seamount basalts of SCS and other late Cenozoic basalts from southeast China (Fig. 5d, e) (Tu et al. 1991, 1992; Flower et al. 1992; Zhang et al. 1996; Zou et al. 2000), which were described as DUPAL anomaly (Hart 1984). However, the Dupal reservoir is characterized by relatively high time-integrated values of Rb/Sr, U/Pb, and Th/U (Hart 1984), which is inconsistent with the relatively low $^{87}Sr/^{86}Sr$ of the EGD Miocene basalts. One possibility is reinjection of small amount of continental crustal material with "Dupal anomaly" features into the mantle source region before eruption. Because the continental crust has much higher Pb concentration than the OIB with comparable Sr, Nd, and Hf concentrations (Hofmann 1997; White 2010), it would

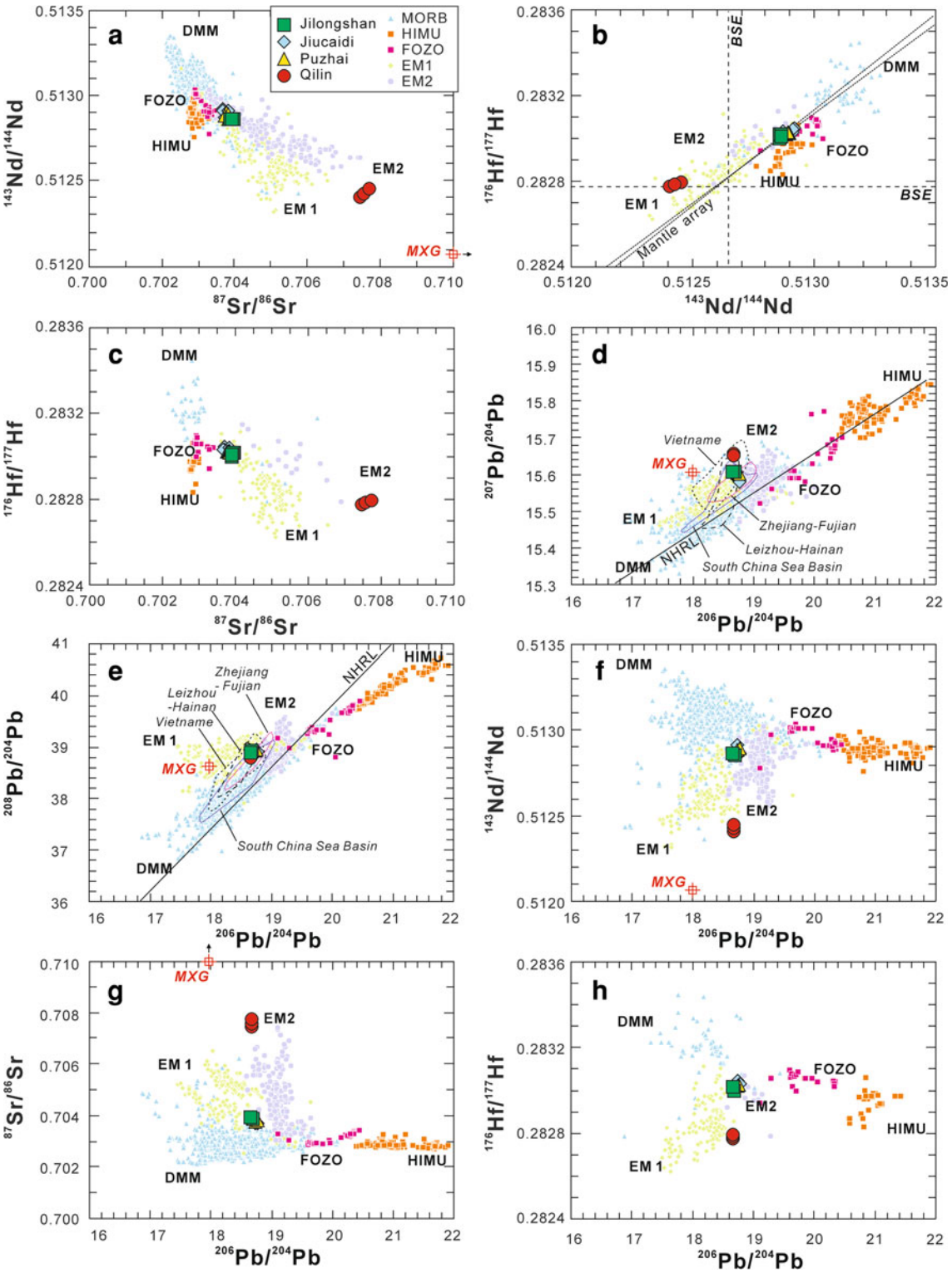

Fig. 5 **a** $^{143}Nd/^{144}Nd$ vs. $^{87}Sr/^{86}Sr$; **b** $^{176}Hf/^{177}Hf$ vs. $^{143}Nd/^{144}Nd$; **c** $^{176}Hf/^{177}Hf$ vs. $^{87}Sr/^{86}Sr$; **d** $^{207}Pb/^{204}Pb$ vs. $^{206}Pb/^{204}Pb$; **e** $^{208}Pb/^{204}Pb$ vs. $^{206}Pb/^{204}Pb$; **f** $^{143}Nd/^{144}Nd$ vs. $^{206}Pb/^{204}Pb$; **g** $^{87}Sr/^{86}Sr$ vs. $^{206}Pb/^{204}Pb$ and **h** $^{176}Hf/^{177}Hf$ vs. $^{206}Pb/^{204}Pb$ for the eastern Guangdong Cenozoic basalts. MXG is felsic granulite xenolith in the Mingxi Cenozoic basalt (Tables 2, 3). Pb isotopic data sources of basalts are as follows: South China Sea Basin (Tu et al. 1992), Zhejiang-Fujian (Zou et al. 2000; Basu et al. 1991), Leizhou-Hainan (Zhu and Wang 1989; Tu et al. 1991), Vietname (Nguyen et al. 1996). Nd–Hf mantle array from Chauvel et al. (2008); Northern Hemisphere Reference Line (NHRL) and mantle source "reservoirs" BSE from Zindler and Hart (1986); the existing Nd, Sr, Pb and Hf isotope data from the MORB-OIB data base compilation of Stracke et al. (2003, 2005)

impart the mantle source with crustal Pb isotopes over Sr–Nd–Hf isotopes. However, the crustal material would also impart the characteristic Pb enrichment and Nb–Ta–Ti depletion, which is not observed in the EGD Miocene OIB-type basalts. Another possibility is that small amount of Dupal-like materials may be present in the lithospheric mantle that had been assimilated prior to the eruption of the EGD Miocene basalts. This is reasonable as the existence of old lithospheric relicts in the uppermost mantle beneath South China had been recognized previously through studies of mantle xenoliths carried out in the Cenozoic basalts in this region (Fan et al. 2000; Xu et al. 2000, 2002).

OIB are much more enriched in incompatible elements than MORB, which had been considered as resulting from the recycled ocean crust (Hofmann and White 1982; Hofmann 1997) or subcontinental lithosphere (McKenzie and O'Nions 1983, 1995). Such fertile mantle source material from depth (asthenospheric source) is compositionally peridotitic and volumetrically dominant (Hofmann 1997; Niu and O'Hara 2003; Niu 2008, 2009; White 2010), but not fully satisfactory in all respects of the geochemical signature of OIB (White 2010). In addition to fertile mantle source material from depth, OIB melts may have the components of the melt layer at top of the seismic low velocity zone (LVZ) and the metasomatic veins formed earlier in the lithosphere (Niu and O'Hara 2003; Niu 2008, 2009). The EGD Miocene OIB basalts have high incompatible trace element abundances (such as Rb, Ba, Th, U, Nb–Ta, and LREE) (Fig. 4b), which indicates an enriched asthenospheric source. However, the EGD Miocene OIB basalts mostly plot in between DMM and EMs (both EM1 and EM2) in Sr–Nd–Hf–Pb isotope spaces (Fig. 5), indicating probably a mixture with the depleted component originally thought to be the depleted mantle.

The depleted mantle would not melt without thermal perturbation or metasomatism. The Paleopacific subduction had a great effect on subcontinental lithosphere mantle beneath South China during the Late Mesozoic (e.g., Zhou et al. 2006), which may produce the enriched veins in the lithosphere. But partial melting of such enriched veins would impart the characteristic Nb–Ta–Ti depletion if the metasomatism took place in mantle wedge environment (Donnelly et al. 2004), which contradicts with the geochemical signature of the EGD Miocene OIB-type basalts. The metasomatic veins in the lithosphere would also be result of prior incipient melt within the LVZ (Niu 2008, 2009), which is consistent with the genesis of DUPAL anomaly in the EGD Miocene basalts. This interpretation is also consistent with the process of the late Mesozoic to Cenozoic melting and subsequent metasomatic enrichment of lithospheric mantle beneath southeastern China (Xu et al. 2002, 2003, 2008).

The near chondritic Nb/Ta ratios (17.1–19.2; Fig. 6a; Supplemental Table 3) of the EGD Miocene OIB-type basalts are apparently decoupled from Zr/Hf ratios (Fig. 6a) in contrast to the correlated variations between these two ratios in some seafloor basalts (Niu and Batiza 1997; Niu et al. 2002) and abyssal peridotites (Niu 2004), while it is possible that partial melting in mantle source regions could cause Nb–Ta and Zr–Hf fractionation, especially if the extent of melting is low (i.e., *Low-F* scenario) (Weyer et al. 2003; Niu 2004; Pfänder et al. 2007). The model calculations show that low-degree partial melting of dominant garnet peridotite assemblages can

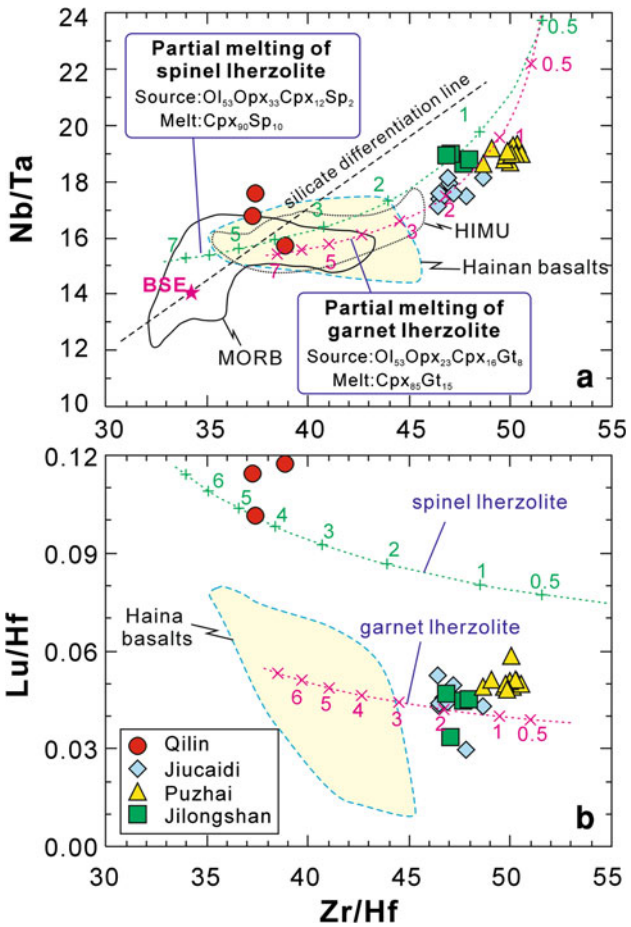

Fig. 6 Nb/Ta and Lu/Hf vs. Zr/Hf of the eastern Guangdong Cenozoic basalts. The silicate differentiation line indicates a first-order coupling of Nb/Ta and Zr/Hf fractionation in terrestrial reservoirs (Münker et al. 2003). The assumed source of non-modal batch melting curves is "99 % primitive mantle + 1 % crust", except for Hf, for which the concentration in the primitive mantle was elevated from 0.3 to 0.38 ppm to fit the requirement of a lower Zr/Hf ratio (Pfänder et al. 2007). Both the primitive mantle and crust values are from Palme and O'Neill (2003). The numbers of the curves denote degree of melting in percent, using the partition coefficients of McDade et al. (2003) (Ol, Opx, Cpx), Westrenen et al. (1999) (Gt) and Elkins et al. (2008) (Sp). HIMU and MORB from Pfänder et al. (2007), BSE value from Münker et al. (2003)

produce the observed range in Zr/Hf and Nb/Ta ratios of the EGD Miocene basalts (Fig. 6).

Eocene Arc-like basalts

The Qilin basalts have high LOI values (Supplemental Table 3) and abundant secondary minerals such as talc and actinolite due to the breakdown of dominant pyroxenes. This secondary alteration results in CaO depletion, MgO enrichment, and varying mobility of LILs (such as Rb, Cs, and Ba) and transition metals (such as Sc, Cr, Co, and Ni) (Wang et al. 2010). Thus, the Qilin samples have relatively high $Mg^{\#}$, but low CaO, Cr, and Ni (Fig. 3; Supplemental Table 3). In contrast, Sm–Nd isotopic systems and incompatible elements such as REE, high field strength elements (HFSEs) Nb–Ta–Ti, and Y are essentially immobile during such alteration (Wang et al. 2010). As plagioclase resists against the alteration, Sr and Pb would be mostly preserved in the rocks, consistent with the extremely similar primitive mantle-normalized multi-element diagrams of the Qilin samples (Fig. 4b).

The Qilin basalts exhibit strong relative depletion of Nb, Ta, and Ti (Fig. 4b) and have enriched Sr–Nd–Hf–Pb isotopic compositions (Fig. 5). Crustal contamination might be a possibility for the negative Ta–Nb–Ti anomalies and enriched Sr–Nd–Hf–Pb isotopes in the Qilin basalts. However, the Qilin pipe is a basaltic dyke with abundant mafic to ultramafic breccias; thus, the basalts ascended rapidly and avoided significant interaction with crust. The crustal contamination, if any, is rather limited and inadequate to explain the large negative Ta–Nb–Ti anomalies in the Qilin basalts.

Fractional crystallization of Ti-bearing minerals such as rutile, ilmenite, or amphibole has notable effect on Ta–Nb–Ti depletion (Tiepolo et al. 2001; Xiong et al. 2005; Klemme et al. 2006). However, the processes of partial melting of unmodified upper mantle peridotite and subsequent crystal fractionation cannot account for the strongly negative Nb–Ta–Ti anomalies and pronounced enrichment of incompatible elements seen in Fig. 4b.

The origin of strong depletion of Ta–Nb–Ti and enriched Sr–Nd–Pb isotopic compositions could also be due to recycled terrigenous sediments in the mantle source region (Peccerillo 1985; Conticelli and Peccerillo 1992; Hawkesworth et al. 1993; Zhao et al. 2009) or supra-subduction zone fluid metasomatism (Tatsumi 1986; Donnelly et al. 2004). However, synchronous slab subduction is unlikely because EGD was far away from the west Pacific subduction zone during Middle Eocene to Miocene (Fig. 1; Lee and Lawver 1995; Zhou et al. 1995). Thus, recycled terrigenous sediments by previous subduction processes (i.e., Paleopacific subduction) might have been responsible for the metasomatism of the mantle source for the Qilin basalts, which might also explain why the Qilin samples have relatively high concentration of K and Pb (Fig. 4b). On the other hand, Sr–Nd–Pb–Hf isotopes of the Qilin basalts show a trend of hybrid mantle source between EM1 and EM2 (Fig. 5), indicating that recurrent upward migration of intraplate melts may overprint the ancient subduction-related enrichment. Overall, the Qilin basalts are likely low-degree partial melting of dominant spinel phase mantle source for their relatively low Zr/Hf ratios but high Lu/Hf ratios (Fig. 6).

Genesis of distinct mantle sources

The distinct geochemical characters between the Eocene Arc-like basalts ($\sim$35.5 Ma) and Miocene OIB-type basalts ($\sim$20 and $\sim$6.6 Ma) in eastern Guangdong suggest that the mantle sources of the basalts changed from principally ancient subduction metasomatized mantle source to dominantly depleted mantle source. Such a mantle source change has been interpreted as reflecting source shift from enriched lithospheric mantle to OIB-type asthenospheric mantle by a process of replacing Archean-Proterozoic lithosphere with asthenosphere during late Mesozoic to Cenozoic (Fan et al. 2000; Xu et al. 2000, 2002, 2003; Zhu et al. 2004). This is in essence a lithosphere-thinning event as inferred to have taken place beneath the North China Craton in the Mesozoic. However, it is not straightforward to invoke lithosphere thinning to explain the source change for the EGD Cenozoic basalts as this process would be accompanied by widespread magmatism (e.g., Xu 2001; Xu et al. 2004). So the lithosphere-thinning-associated magmatism would have taken place before the eruption of Qilin basalts.

On the other hand, mantle xenoliths in Qilin basalts show a stratified mantle lithosphere. The upper portion contains features of strong metasomatism of melt/fluid of highly variable composition, while the deep portion is moderately depleted peridotites with trace element signatures of incipient metasomatism (Xu et al. 2002). Thus, the Eocene Arc-like basalts (35.5 $\pm$ 0.4 Ma) were likely generated from the lithospheric mantle that had been mostly affected by metasomatism of ancient melt/fluid (Xu et al. 2000, 2002). The preferential melting of metasomatism components of the deep portion of the lithosphere can also be responsible for the stratified mantle lithosphere. Additionally, the high and flat heavy REE patterns in Qilin basalts (Fig. 4a) may indicate a relatively shallow source corresponding to the lithosphere-thinning taking place during late Mesozoic to early Cenozoic (Zhu et al. 2004). The anomalously high geotherm at shallow depths established by mantle xenoliths in Qilin basalts (Huang and Xu 2010) may reflect the possibility of partial melting at shallow lithospheric mantle in response to the early phase of the lithosphere rifting.

In contrast, the EGD Miocene OIB basalts resulted from partial melting of the asthenospheric mantle. Such melt may have assimilated metasomatic veins formed earlier in the lithosphere (Xu et al. 2002). The low and steep heavy REE patterns in the Miocene OIB basalts (Fig. 4a) are all consistent with derivation dominantly from greater depths in the garnet peridotite facies (Fig. 6, 7). Specifically, the youngest Jilongshan basalts (6.64 ± 0.07 Ma) have lower and steeper HREE patterns than the Puzhai and Jiucaidi basalts (Fig. 4a). Because containing higher Ni, but lower Cr, SiO_2, and Al_2O_3 than the Jiucaidi (20.8 ± 0.1 Ma), Puzhai (20.2 ± 0.1 Ma), and Hainan basalts (~13 Ma; Wang et al. 2012) at a given $Mg^{\#}$ (such as $Mg^{\#} = 0.60$; Fig. 3), the Jilongshan basalts would be derived from a more peridotitic source. Thus, the increased garnet-residual signature in the Jilongshan basalts reflects a larger proportion of melts derived from the garnet peridotite facies (Fig. 7), indicating the deeper magma source.

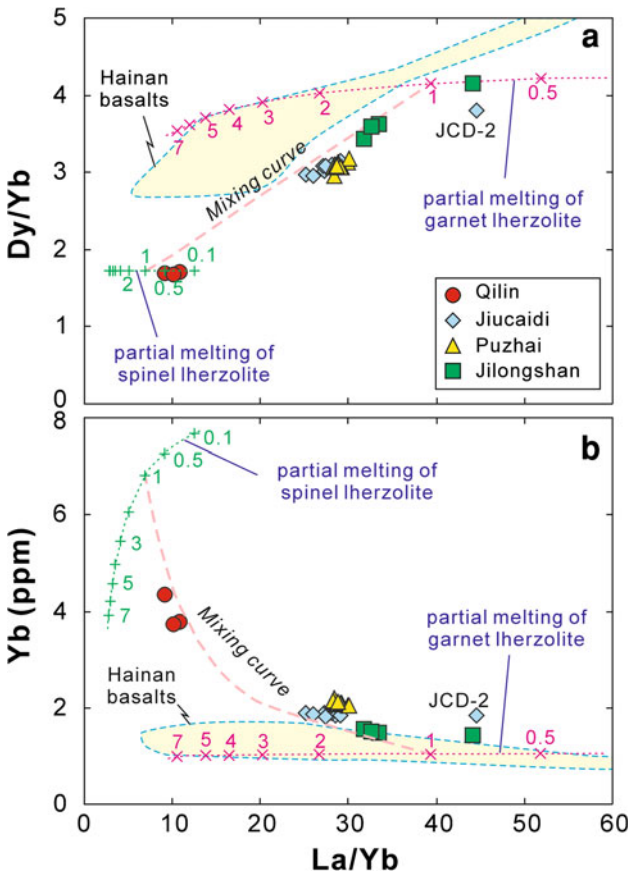

Fig. 7 Plots of Dy/Yb, Yb vs. La/Yb for the eastern Guangdong Cenozoic basalts. Non-modal batch melting curves were calculated using partition coefficients from McKenzie and O'Nions (1991). The source and melt mineral modes are as Fig. 6

Evolution of the Cenozoic lithospheric mantle beneath SE China

During Late Cretaceous–Eocene, the southeastern margin of South China was in an extension regime (Ren et al. 2002). Many authors also link the early seafloor spreading stage of the SCS to lithospheric extension of South China (Fig. 1), and the Paleogene volcanic activities for the lithospheric extension migrated southwards and eventually led to the seafloor spreading of the SCS during ~32–16 Ma (Ru and Pigott 1986; Hayes et al. 1995; Chung et al. 1997; Xu et al. 2002). For this reason, Cenozoic basaltic rocks of SE China associated closely with major regional faults (Fig. 1) are interpreted as relating to continental extension (e.g., Chung et al. 1994, 1997; Liu et al. 1994; Qi et al. 1994; Zou et al. 2000; Ho et al. 2003). However, some studies also suggested that the widespread basaltic volcanism in SE China and the inception of Cenozoic basins such as Shanshui and SCS basins resulted from upwelling of a mantle plume (Deng et al. 2004; Xiao et al. 2004; Zhou et al. 2009). Thus, the geodynamic mechanism and lithospheric evolution of SE China during the late Cenozoic remain debatable. Geochemical variation in the EGD basalts pre-, during, and post-opening of SCS may offer some perspectives on the evolution of the Cenozoic lithospheric mantle beneath SE China.

Cretaceous mafic dikes from Northern Guangdong of SE China, interpreted as the results of the episodes of extensional activities (~140, ~124, ~105 and ~90 Ma) in SE China, show arc signatures or OIB features in their trace elements with variable $\varepsilon_{Nd}(t)$ from −5.9 to +5.2 (Fig. 8) (Li et al. 1997). Cretaceous extension in SE China was followed by the generation of pull-apart basins with

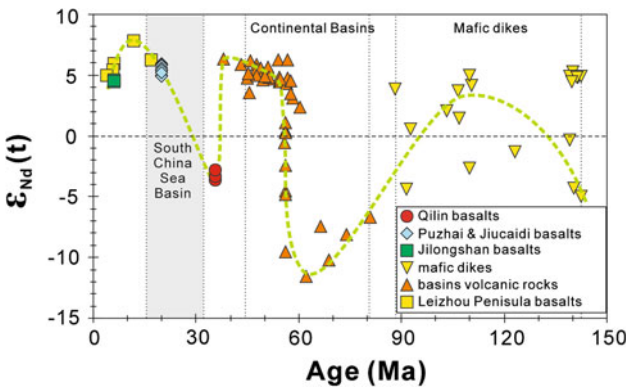

Fig. 8 Temporal variation in the Nd isotopic composition of the basaltic rocks at SE China margin from the late Mesozoic to Cenozoic. Mafic dikes from Li et al. (1997), bimodal volcanic rocks in extensional basins from Chung et al. (1997), Zhu et al. (2004) and Zhou et al. (2009), Leizhou Penisula basalts from Zhu et al. (2004)

large-scale bimodal volcanism consisting of intraplate tholeiitic basalt and trachyte/rhyolite associations during the Late Cretaceous and early Eocene (Chung et al. 1997; Zhu et al. 2004; Zhou et al. 2009). These bimodal volcanic rocks of the basins changed in geochemical features (especially in initial Nd isotopes) at 56 ± 2 Ma (Fig. 8) (Zhu et al. 2004). The earlier volcanic rocks have enriched Nd isotopes with negative $\varepsilon_{Nd}(t)$ of −11.5 to −6.5, while the younger volcanic rocks show depleted features with positive $\varepsilon_{Nd}(t)$ of +3.1 to +6.4 (Fig. 8) (Chung et al. 1997, Zhu et al. 2004; Zhou et al. 2009). Thus, Cretaceous to early Eocene mafic rocks of SE China might be derived from the hybrid mantle sources including asthenosphere and metasomatic lithosphere (Fig. 9a). But there is an obvious trend of sources from dominantly metasomatic lithosphere at an early stage to asthenosphere at the main stage of the extension (Fig. 8). The basement heat flow increased during crustal extension (He et al. 2001), indicating that the evolution of these basins was accompanied by the thinning of lithospheric mantle, upwelling of the asthenosphere and a large-scale bimodal volcanism (Fig. 9a).

During the late Eocene, the EGD lithosphere might have been largely thinned by basal convective removal as suggested by the shallow mantle source of Qilin Arc-type basalts (~35.5 Ma) and anomalously high geotherm indicated by Qilin mantle xenoliths (Xu et al. 1996; Huang and Xu 2010). At this stage, partial melting of the asthenosphere may be limited because of the prior depletion of volatile-rich component generating widespread basaltic volcanism in SE China during Late Cretaceous to Early Eocene (Chung et al. 1997, Zhu et al. 2004; Zhou et al. 2009). However, low-degree partial melting of metasomatic relicts in the deep portion of the lithosphere occurred because of the relatively high conductive heat transfer (Fig. 9b) as manifested by the high geotherm (Xu et al. 1996; Huang and Xu 2010), the stratified mantle lithosphere (Xu et al. 2002), and the extremely enriched Sr–Nd–Pb–Hf isotopes of the Qilin basalts (Fig. 5). This interpretation is consistent with the model calculation results that the Qilin basalts would be the low-degree partial melting of a dominant spinel peridotite facies conditions (Figs. 6, 7). With the elimination of metasomatic relicts in the lithospheric mantle, the wet solidus would shift toward the dry solidus

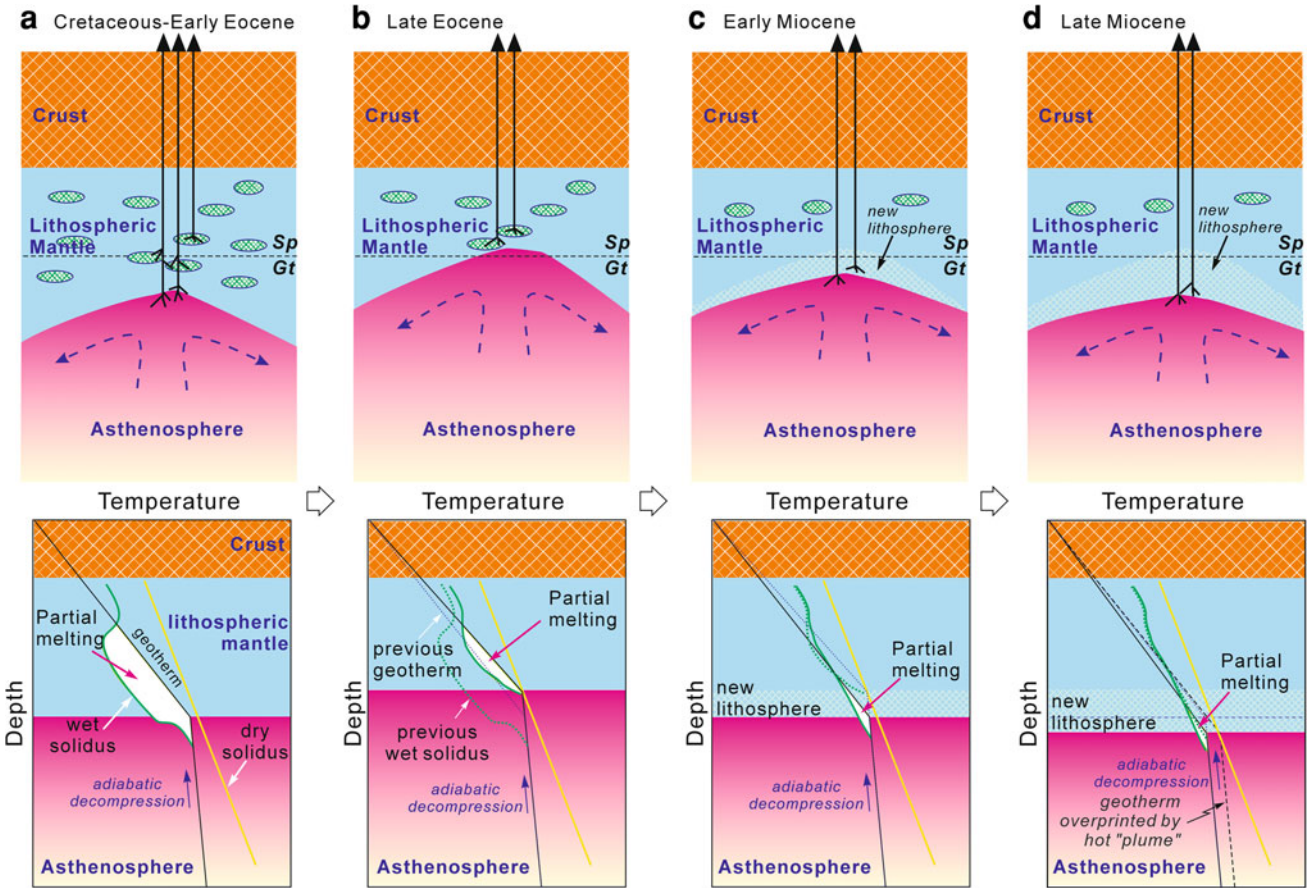

Fig. 9 Schematic diagram illustrating the evolution of lithospheric mantle beneath SE China during late Mesozoic to Cenozoic

and the partial melting would stop finally without additional heat source. With the conductive heat loss to the surface since the extension stopped (He et al. 2001; Huang et al. 2007), the lithosphere will thicken with time by accreting the subjacent volatile (e.g. H_2O, CO_2, etc.) and incompatible element enriched LVZ material at its base (Niu 2008; Niu and O'Hara 2008, 2009; Huang et al. 2010), a process that leads to the formation of metasomatized veins within the mantle lithosphere which do not melt without future thermal perturbation (Niu 2008). But the refertilized (metasomatized) mantle lithosphere would begin partial melting when the geotherm intersects the new wet solidus as the asthenosphere ascends in response to temporary lithosphere extension during the seafloor spreading of South China Sea (Fig. 9c). Attributed to low-degree partial melting of a recently metasomatized mantle source, the Jiucaidi and Puzhai basalts (~20 Ma) at this stage are all enriched in incompatible trace elements, but have relatively depleted Sr–Nd–Hf isotopes. The low-degree partial melting and scattered magmatism at this stage (Ho et al. 2003 and this current paper) would not induce thinning of lithosphere beneath the continental margin of SE China. On the contrary, the lithosphere would continue thickening through basal accretion of the LVZ material. Similarly, the refertilized mantle lithosphere may melt when the asthenosphere (Fig. 9d) was influenced by the Hainan mantle plume (Lei et al. 2009; Wang et al. 2012). Consequently, the Jilongshan OIB-type basalts (~6.6 Ma) at this stage have deeper magma source than the Puzhai and Jiucaidi basalts (~20 Ma) with similar Sr–Nd–Pb–Hf isotopes. Volumetrically insignificant magmatism with OIB-type signature had taken place since the late Miocene in SE China and the broad region, including the Hainan Island, Leizhou Peninsula, and Taiwan Strait, all associated with pre-existing zones of lithosphere weakness (Fig. 1a).

Implication for the continental rift during the lithospheric extension

Studies of the evolution of continental rift systems and rifted continental margins have led to the development of many hypotheses for the driving forces which create them (McKenzie 1978; Keen 1985; Bache et al. 2010). Rifting could be classified into active and passive (Sengör and Burke 1978). Active or passive continental rifting is all associated with thinning of the lithosphere, ascent of the asthenosphere, and decompression melting. The controversy exists as to whether rift zones are produced by upwelling mantle splitting the continent along pre-existing zones of weakness (active models) or whether the mantle rises passively in response to lithospheric extension (passive models) (Spohn and Schubert 1982). Therefore, active rifting would be associated with dynamic mantle upwelling, large-scale topographic uplift, and melt generation prior to the actual rifting, whereas passive rifting is accompanied by lithosphere thinning and magmatism as a result of extension-induced asthenospheric upwelling and decompression melting without topographic swells prior to rifting (Ruppel 1995; Schmeling 2010).

The basalts at EGD revealed a process of lithospheric thickening beneath SE China since late Eocene accompanied by temporary low-degree partial melting of asthenosphere by decompression. As results, there are only scattered volcanic pipes surfaced (vs. larger scale flows) at the continental margin of SE China pre- and during the seafloor spreading of South China Sea. These observations are apparently inconsistent with the standard mantle plume model which is expected to be associated with high heat flow, broad zones of regional uplift, and widespread magmatism (e.g., Campbell 2001). Thus, the limited basaltic magmatism manifested by very few scattered volcanic pipes without extensive magmatism at the continental margin of SE China during late Eocene–early Miocene indicates that the seafloor spreading of the South China Sea during 32–16 Ma may not be caused by a mantle plume, but probably resulted from lithosphere extension-induced rifting, accompanied lithosphere thinning, asthenosphere passive upwelling, and basaltic magmatism. This is consistent with the southward ridge jump and the SCS ridge orientation parallel to the coastline of South China but perpendicular the Pacific and Philippine subduction zone (Fig. 1a).

Therefore, the evolution of lithospheric mantle at the continental margin of SE China, indicated by the geochemical features of the EGD basalts during the late Eocene–early Miocene, records the development of a typical passive continental margin through rifting and evolution to an oceanic basin. Furthermore, the potential "Hainan mantle plume" (Wang et al. 2012), if it existed, may have surfaced through basaltic magmatism as a result of lithosphere extension and thinning, as manifested by OIB-type magmatism on the Hainan Island, Leizhou Peninsula, in the Taiwan Strait as well as the continental margin in the SE China since the late Miocene. That is, it is the lithospheric extension and thinning in the broad SE China-South China Sea Region that resulted in the development of the marginal seas, including the South China Sea, and allowed the "Hainan" mantle plume to express. The SCS seafloor spreading during ~32–16 Ma would have drained mantle melts of plume origin as well as lithosphere extension-induced melt, which explains why basaltic magmatism is rare in this period of time in the peripheral region except for the leakage in a few places as Qilin, Puzhai, and Jiucaidi we study here. This is wholly consistent with the more widespread magmatism around the SCS before and after SCS seafloor spreading (Ho et al.

2003; Zhu et al. 2004). The late Miocene basalts in the Hainan Island, Leizhou Peninsula, and Taiwan Strait are dominated by tholeiitic phases (Zou et al. 2000; Ho et al. 2003; Wang et al. 2012), which would be attributed to large-scale lithosphere extension and thinning in the pre-existing lithosphere weakness zones of the SE China.

Conclusion

The ^{40}Ar–^{39}Ar chronology, whole rock trace elements, and Sr–Nd–Pb–Hf isotopes of Cenozoic basalts from eastern Guangdong facilitate our understanding of the mantle evolution at the continental margin of SE China from the late Eocene to late Miocene, which corresponds to the period of active seafloor spreading of the South China Sea.

There are three episodes of Cenozoic basaltic magmatism (35.5, ~20 and 6.6 Ma) with distinctive trace element and Sr–Nd–Hf–Pb isotope characteristics in eastern Guangdong. The Qilin arc-like basalts at 35.5 Ma are partial melting of relict ancient metasomatized mantle lithosphere. Both the early and late Miocene OIB-type basalts (~20) are low-degree partial melting of the dominant asthenospheric mantle at different depths.

There is an overall lithospheric thickening process beneath SE China from the late Eocene to late Miocene, recording a passive continental margin that formed the marginal basin with seafloor spreading.

Acknowledgments We gratefully acknowledge the constructive comments of C. Beier and X. C. Wang, which considerably improved the manuscript. We thank X. R. Liang, Y. Liu, and X. L. Tu for analytical assistance. This research was supported by the Knowledge Innovation Projects of the Chinese Academy of Sciences (KZCX1-YW-15-2, KZCX2-YW-QN106), the National Science Foundation of China (NSFC Projects 40773015, 91014003, 41130314, 41121002) and the CAS/SAFEA International Partnership Program for Creative Research Teams (KZCX2-YW-Q04-06). This is contribution No. IS-1561 from GIG-CAS.

References

Bache F, Olivet JL, Gorini C, Aslanian D, Labails C, Rabineau M (2010) Evolution of rifted continental margins: the case of the Gulf of Lions (Western Mediterranean basin). Earth Planet Sci Lett 292:345–356

Baker J, Waight T (2002) Pb isotope analysis using Tl and a ^{207}Pb-^{204}Pb spike on a double focusing MC-ICPMS. Geochim Cosmochim Acta 66(15A):A44

Basu AR, Wang JW, Huang WK, Xie GH, Tatsumoto M (1991) Major element, REE, and Pb, Nd and Sr isotopic geochemistry of Cenozoic volcanic rocks of eastern China: implications for their origin from sub-oceanic type mantle reservoirs. Earth Planet Sci Lett 105:149–169

BGMR (Bureau of Geology and Mineral Resources) (1974) Geological map of Guangdong Province. Sheet F-50-III (Shangtou), scale 1: 200,000

Bouvier A, Vervoort JD, Patchett PJ (2008) The Lu-Hf and Sm-Nd isotopic composition of CHUR: constraints from unequilibrated chondrites and implications for the bulk composition of terrestrial planets. Earth Planet Sci Lett 273:48–57

Briais A, Patriat P, Tapponnier P (1993) Updated interpretation of magnetic anomalies and seafloor spreading stages in the South China Sea: implication for the Tertiary tectonics of Southeast Asia. J Geophys Res 98(B4):6299–6328

Campbell IH (2001) Identification of ancient mantle plumes. In: Ernst RE, Buchan KL (eds) Mantle plumes: their identification through time. Geological Society of America Special Papers 352:5–22

Chauvel C, Lewin E, Carpentier M, Arndt NT, Marini JC (2008) Role of recycled oceanic basalt and sediment in generating the Hf–Nd mantle array. Nat Geosci 1:64–67

Chung SL, Sun S-s TuK, Chen C-H, Lee CY (1994) Late Cenozoic basaltic volcanism around the Taiwan strait, SE China: product of lithosphere-asthenosphere interaction during continental extension. Chem Geol 112:1–20

Chung SL, Cheng H, Jahn BM, O'Reilly SY, Zhu BQ (1997) Major and trace element, and Sr-Nd isotope constraints on the origin of Paleogene volcanism in South China prior to the South China Sea opening. Lithos 40:203–220

Conticelli S, Peccerillo A (1992) Petrology and geochemistry of potassic and ultrapotassic volcanism in central Italy: petrogenesis and inferences on the evolution of the mantle sources. Lithos 28:221–240

Deng JF, Mo XX, Zhao HL, Wu ZX, Luo ZH, Su SG (2004) A new model for the dynamic evolution of Chinese lithosphere: "continental roots-plume tectonics". Earth-Sci Rev 65:223–275 (in Chinese with English abstract)

Donnelly KE, Goldstein SL, Langmuir CH, Spiegelman M (2004) Origin of enriched ocean ridge basalts and implications for mantle dynamics. Earth Planet Sci Lett 226:347–366

Elkins LJ, Gaetani GA, Sims KWW (2008) Partitioning of U and Th during garnet pyroxenite partial melting: constraints on the source of alkaline ocean island basalts. Earth Planet Sci Lett 265:270–286

Fan WM, Zhang HF, Baker J, Javis KE, Mason PRD, Menzies MA (2000) On and off the North China craton: where is the Archean keel? J Petrol 41:933–950

Flower MFJ, Zhang M, Chen CY, Tu K, Xie GH (1992) Magmatism in the South China Basin 2: post-spreading quaternary basalts from Hainan Island, South China. Chem Geol 97:65–87

Griffin WL, Pearson NJ, Belousova E, Jackson SE, O'Reilly SY, van Achterberg E, Shee SR (2000) The Hf isotope composition of cratonic mantle: LAM-MC-ICPMS analysis of zircon megacrysts in kimberlites. Geochim Cosmochim Acta 64:133–147

Hart SR (1984) A large-scale isotope anomaly in the Southern Hemisphere mantle. Nature 309:753–757

Hawkesworth CJ, Gallagher K, Hergt JM, McDermott F (1993) Mantle and slab contributions in arc magmas. Annu Rev Earth Planet Sci 21:175–204

Hayes DE, Nissen SS, Buhl P (1995) Through going crustal faults along the margin of Southern China Sea and their role in the crustal extension. J Geophys Res 100(B11):22435–22446

He LJ, Wang KL, Xiong LP, Wang JY (2001) Heat flow and thermal history of the South China Sea. Phys Earth Planet Inter 126: 211–220

Ho KS, Chen JC, Lo CH, Zhao HL (2003) ^{40}Ar-^{39}Ar dating and geochemical characteristics of late Cenozoic basaltic rocks from the Zhejiang-Fujian region, SE China: eruption ages, magma evolution and petrogenesis. Chem Geol 197:287–318

Hofmann AW (1997) Mantle geochemistry: the message from oceanic volcanism. Nature 385:219–229
Hofmann AW, White WM (1982) Mantle plumes from ancient oceanic crust. Earth Planet Sci Lett 57:421–436
Huang XL, Xu YG (2010) Thermal state and structure of the lithosphere beneath eastern China: a synthesis on basalt-borne xenoliths. J Earth Sci 21:711–730
Huang XL, Xu YG, Lo CH, Wang RC, Lin CY (2007) Exsolution lamellae in a clinopyroxene megacryst aggregate from Cenozoic basalt, Leizhou peninsula, South China: petrography and chemical evolution. Contrib Mineral Petrol 154:691–705
Huang XL, Niu YL, Xu YG, Chen LL, Yang QJ (2010) Mineralogical and geochemical constraints on the petrogenesis of post-collisional potassic and ultrapotassic rocks from western Yunnan, SW China. J Petrol 51:1617–1654
Keen MJ (1985) The dynamics of rifting: deformation of the lithosphere by active and passive driving forces. Geophy J Royal Astro Soc 80:95–120
Kelemen PB, Hanghøj K, Greene AR (2003) One view of the geochemistry of subduction-related magmatic arcs, with an emphasis on primitive andesite and lower crust. In: Rudnick RL (ed) The crust, treatise on geochemistry, vol 3. Elsevier, Oxford, pp 593–659
Klemme S, Gunther D, Hametner K, Prowatke S, Zack T (2006) The partitioning of trace elements between ilmenite, ulvospinel, armalcolite and silicate melts with implications for the early differentiation of the moon. Chem Geol 234:251–263
Koppers AAP (2002) ArArCALC: software for $^{40}Ar/^{39}Ar$ age calculations. Comp Geosci 28:605–619
Le Maitre RW (1989) A classification of igneous rocks and glossary of terms: recommendation of the IOU subcommission on the systematics of igneous rocks. Blackwell, Oxford
Lee TY, Lawver LA (1995) Cenozoic plate reconstruction of Southeast Asia. Tectonophys 251:85–138
Lei J, Zhao D, Steinberger B, Wu B, Shen F, Li Z (2009) New seismic constraints on the upper mantle structure of the Hainan plume. Phys Earth Planet Inter 173:33–50
Li XH, Hu RZ, Rao B (1997) Geochronology and geochemistry of Cretaceous mafic dikes from northern Guangdong, SE China. Geochimica 26:14–31 (in Chinese with English abstract)
Li XH, Qi CS, Liu Y, Liang XR, Tu XL, Xie LW, Yang YH (2005) Petrogenesis of the Neoproterozoic bimodal volcanic rocks along the western margin of the Yangtze Block: new constraints from Hf isotopes and Fe/Mn ratios. Chin Sci Bull 50:2481–2486
Liu CQ, Masuda A, Xie GH (1994) Major- and trace-element composition of Cenozoic basalts in eastern China: petrogenesis and mantle source. Chem Geol 114:19–42
McDade P, Blundy JD, Wood BJ (2003) Trace element partitioning on the Tinaquillo Lherzolite solidus at 1.5 GPa. Phys Earth Planet Inter 139:129–147
McKenzie D (1978) Some remarks on the development of sedimentary basins. Earth Planet Sci Lett 40:25–32
McKenzie D, O'Nions RK (1983) Mantle reservoirs and ocean island basalts. Nature 301:229–231
McKenzie D, O'Nions RK (1991) Partial melt distributions from inversion of rare earth element concentrations. J Petrol 32:1021–1091
McKenzie D, O'Nions RK (1995) The source regions of ocean island basalts. J Petrol 36:133–159
Münker C, Pfänder JA, Weyer S, Büchl A, Kleine T, Mezger K (2003) Evolution of planetary cores and the Earth-Moon system from Nb/Ta systematics. Science 301:84–87
Nguyen H, Flower MFJ, Carlson RW (1996) Major, trace element, and isotopic compositions of Vietnamese basalts: interaction of hydrous EM1-rich asthenosphere with thinned Eurasian lithosphere. Geochim Cosmochim Acta 60:4329–4351
Niu YL (2004) Bulk-rock major and trace element compositions of abyssal peridotites: implications for mantle melting melt extraction and post-melting processes beneath ocean ridges. J Petrol 45:2423–2458
Niu YL (2008) The origin of Alkaline lavas. Science 320:883–884
Niu YL (2009) Some basic concepts and problems on the petrogenesis of intra-plate ocean island basalts. Chin Sci Bull 54:4148–4160
Niu YL, Batiza R (1997) Trace element evidence from seamounts for recycled oceanic crust in the eastern equatorial Pacific mantle. Earth Planet Sci Lett 148:471–484
Niu YL, O'Hara MJ (2003) origin of ocean island basalts: a new perspective from petrology, geochemistry, and mineral physics considerations. J Geophys Res 108(B4):2209, doi:10.1029/2002JB002048
Niu YL, O'Hara MJ (2008) Global correlations of ocean ridge basalt chemistry with axial depth: a new perspective. J Petrol 49: 633–664
Niu YL, O'Hara MJ (2009) MORB mantle hosts the missing Eu (Sr, Nb, Ta and Ti) in the continental crust: new perspectives on crust-mantle differentiation and chemical structure of oceanic upper mantle. Lithos 112:1–17
Niu YL, Regelous M, Wendt JI, Batiza R, O'Hara MJ (2002) Geochemistry of near-EPR seamounts: importance of source vs. process and the origin of enriched mantle component. Earth Planet Sci Lett 199:327–345
Palme H, O'Neill HStC (2003) Cosmochemical estimates of mantle composition. In: Carlson RW (ed) The mantle and core, treatise on geochemistry, vol 2. Elsevier, Oxford, pp 1–38
Peccerillo A (1985) Roman Comagmatic Province (Central Italy): evidence for subduction related magma genesis. Geology 13: 103–106
Pfänder JA, Münker C, Stracke A, Mezger K (2007) Nb/Ta and Zr/Hf in ocean island basalts–implications for crust–mantle differentiation and the fate of Niobium. Earth Planet Sci Lett 254:158–172
Qi Q, Taylor LA, Zhou XM (1994) Geochemistry and petrogensis of three series of Cenozoic basalts from southeastern China. Inter Geol Rev 36:435–451
Ren JY, Tamaki K, Li ST, Zhang J (2002) Late Mesozoic and Cenozoic rifting and its dynamic setting in Eastern China and adjacent areas. Tectonophys 344:175–205
Ru K, Pigott JD (1986) Episodic rifting and subsidence in the South China Sea. Assoc Petrol Geol Bull 70:1136–1155
Ruppel C (1995) Extensional processes in continental lithosphere. J Geophys Res 100(B12):24187–24215
Schmeling H (2010) Dynamic models of continental rifting with melt generation. Tectonophys 480:33–47
Sengör AMC, Burke K (1978) Relative timing of rifting and volcanism on earth and its tectonic implications. Geophys Res Lett 5:419–421
Söderlund U, Patchett PJ, Vervoort JD, Isachsen CE (2004) The ^{176}Lu decay constant determined by Lu-Hf and U-Pb isotope systematics of Precambrian mafic intrusions. Earth Planet Sci Lett 219:311–324
Spohn T, Schubert G (1982) Convective thinning of the lithosphere: a mechanism for the initiation of continental rifting. J Geophys Res 87:4669–4681
Stracke A, Bizimis M, Salters VJM (2003) Recycling oceanic crust: quantitative constraints. Geochem Geophys Geosyst 4:8003. doi:10.1029/2001GC000223
Stracke A, Hofmann AW, Hart SR (2005) FOZO, HIMU, and the rest of the mantle zoo. Geochem Geophys Geosyst 6:Q05007. doi:10.1029/2004GC000824
Sun S-S, McDonough WF (1989) Chemical and isotopic systematics of oceanic basalts: implications for mantle composition and processes. In: Saunders AD, Norry MJ (eds) Magmatism in the

Ocean Basins. Geological Society, London, Special Publication 42:313–345
Sun Z, Zhong ZH, Keep M, Zhou D, Cai DS, Li XS, Wu SM, Jiang JQ (2009) 3D analogue modeling of the South China Sea: a discussion on breakup pattern. J Asian Earth Sci 34:544–556
Tannaka T, Togashi S, Kamioka H, Amakawa H, Kagami H, Hamamoto T, Yuhara M, Orihashi Y, Yoneda S, Shimizu H, Kunimaru T, Takahashi K, Yanagi T, Nakano T, Fujimaki H, Shinjo R, Asahara Y, Tanimizu M, Dragusanu C (2000) JNdi-1: a neodymium isotopic reference in consistency with LaJolla neodymium. Chem Geol 168:279–281
Tatsumi Y (1986) Formation of the volcanic front in subduction zones. Geophys Res Lett 13:717–720
Taylor SR, McLennan SM (1985) The continental crust: its composition and evolution. Blackwell Scientific, Oxford
Tiepolo M, Bottazzi P, Foley SF, Oberti R, Vannucci R, Zanetti A (2001) Fractionation of Nb and Ta from Zr and Hf at mantle depths: the role of titanian pargasite and kaersutite. J Petrol 42:221–232
Tu K, Flower MFJ, Carlson RW, Zhang M, Xie G (1991) Sr, Nd and Pb isotopic compositions of Hainan Basalts (South China): implications for subcontinental lithosphere Dupal source. Geology 19:567–569
Tu K, Flower MFJ, Carlson RW, Xie GH, Chen CY, Zhang M (1992) Magmatism in the South China Basin: 1. Isotopic and trace element evidence for an endogenous Dupal mantle component. Chem Geol 97:47–63
Wang XC, Li XH, Li ZX, Liu Y, Yang YH (2010) The Willouran basic province of South Australia: its relation to the Guibei large igneous province in South China and the breakup of Rodinia. Lithos 119:569–584
Wang XC, Li ZX, Li XH, Li J, Liu Y, Long WG, Zhou JB, Wang F (2012) Temperature, pressure, and composition of the mantle source region of Late Cenozoic basalts in Hainan Island, SE Asia: a consequence of a young thermal mantle plume close to subduction zones? J Petrol 53:177–233
Wei GJ, Liang XR, Li XH, Liu Y (2002) Precise measurement of Sr isotopic compositions of liquid and solid base using (LA) MC-ICP-MS. Geochimica 31:295–305 (in Chinese with English abstract)
Westrenen WV, Blundy J, Wood B (1999) Crystal-chemical controls on trace element partitioning between garnet and anhydrous silicate melt. Am Mineral 84:838–847
Weyer S, Münker C, Mezger K (2003) Nb/Ta, Zr/Hf and REE in the depleted mantle: implications for the differentiation history of the crust-mantle system. Earth Planet Sci Lett 205:309–324
White WM (2010) Oceanic island basalts and mantle plumes: the geochemical perspective. Annu Rev Earth Planet Sci 38:133–160
Wilson M (1989) Igneous petrogenesis. Unwin Hyman, London
Windley BF (1995) The evolving continents, 3rd edn. Wiley, Chichester
Xiao L, Wang FZ, Wang H, Pirajno F (2004) The formation of Songliao basin and Bohaiwan basin, northern China: mantle plume tectonic control. Earth Sci J China Univ Geosci 29:283–292 (in Chinese with English abstract)
Xiong XL, Adam J, Green TH (2005) Rutile stability and rutile/melt HFSE partitioning during partial melting of hydrous basalt: implications for TTG genesis. Chem Geol 218:339–359
Xu YG (2001) Thermo-tectonic destruction of the Archaean lithospheric keel beneath the Sino-Korean craton in China: evidence, timing and mechanism. Phys Chem Earth (A) 26:747–757
Xu XS, O'Reilly SY, Zhou XM, Griffin WL (1996) A xenolith-derived geotherm and the crust-mantle boundary at Qilin, southeastern China. Lithos 38:41–62
Xu XS, O'Reilly SY, Griffin WL, Zhou XM (2000) Genesis of young lithospheric mantle in the southeastern China: a LAM-ICPMS trace element study. J Petrol 41:111–148
Xu YG, Sun M, Yan W, Liu Y, Huang XL, Chen XM (2002) Xenolith evidence for polybaric melting and stratification of the upper mantle beneath South China. J Asian Earth Sci 20:937–954
Xu XS, O'Reilly SY, Griffin WL, Zhou XM (2003) Enrichment of upper mantle peridotite: petrological, trace element and isotopic evidence in xenoliths from SE China. Chem Geol 198:163–188
Xu YG, Huang XL, Ma JL, Wang YB, Iizuka Y, Xu JF, Wang Q, Wu XY (2004) Crustal-mantle interaction during the thermo-tectonic reactivation of the North China Craton: SHRIMP zircon U-Pb age, petrology and geochemistry of Mesozoic plutons in western Shandong. Contrib Mineral Petrol 147:750–767
Xu XS, Griffin WL, O'Reilly SY, Pearson NJ, Geng HY, Zheng JP (2008) Re-Os isotopes of sulfides in mantle xenoliths from eastern China: progressive modification of lithsopheric mantle. Lithos 102:43–64
Zhang M, Tu K, Xie GH, Flower MFJ (1996) Subduction-modified subcontinental mantle in South China: trace element and isotope evidence in basalts from Hainan Island. Chinese J Geochem 15:1–19
Zhao ZD, Mo XX, Dilek Y, Niu YL, DePaolo DJ, Robinson P, Zhu DC, Sun CG, Dong GC, Zhou S, Luo ZH, Hou ZQ (2009) Geochemical and Sr-Nd-Pb-O isotopic compositions of the post-collisional ultrapotassic magmatism in SW Tibet: petrogenesis and implications for India intra-continental subduction beneath southern Tibet. Lithos 113:190–212
Zhou D, Ru K, Chen HZ (1995) Kinematics of Cenozoic extension on the South China Sea continental margin and its implications for the tectonic evolution of the region. Tectonophys 251:161–177
Zhou XM, Sun T, Shen WZ, Shu LS, Niu YL (2006) Petrogenesis of Mesozoic granitoids and volcanic rocks in South China: a response to tectonic evolution. Episodes 29:26–33
Zhou H, Xiao L, Dong Y, Wang C, Wang F, Ni P (2009) Geochemical and geochronological study of the Sanshui basin bimodal volcanic rock suite, China: implications for basin dynamics in southeastern China. J Asian Earth Sci 34:178–189
Zhu BQ, Wang H (1989) Nd-Sr-Pb isotopic and chemical evidence for the volcanism with MORB-OIB source characteristics in the Leiqiong area, China. Geochimica 3:193–201 (in Chinese with English abstract)
Zhu BQ, Wang HF, Chen YW, Chang XY, Hu YG, Xie J (2004) Geochronological and geochemical constraint of the Cenozoic extension of Cathaysian lithosphere and tectonic evolution of the border sea basins in East Asia. J Asian Earth Sci 24:163–175
Zindler A, Hart S (1986) Chemical geodynamics. Annu Rev Earth Planet Sci 14:493–571
Zou HB, Zindler A, Xu XS, Qi Q (2000) Major, trace element, and Nd, Sr and Pb isotope studies of Cenozoic basalts in SE China: mantle sources, regional variations, and tectonic significance. Chem Geol 171:33–47